STUDY

OF

STOCHASTIC PROCESSES AND RNA ELASTICITY

USING OPTICAL TWEEZERS

by

Yeonee Seol

A Dissertation Submitted to the Faculty of the

DEPARTMENT OF PHYSICS

In Partial Fulfillment of the Requirements
For the Degree of

DOCTOR OF PHILOSOPHY

In the Graduate College

THE UNIVERSITY OF ARIZONA

2004

The University of Arizona ®
Graduate College

As members of the Final Examination Committee, we certify that we have read the dissertation prepared by Yeonee Seol

entitled Study of stochastic processes and RNA elasticity using optical tweezers

and recommend that it be accepted as fulfilling the dissertation requirement for the Degree of Doctor of philosophy

Koen Visscher	4/8/04 date
Michael F. Brown	04/08/04 date
Robert S. Maier	4/8/04 date
Srinivas Manne	4/8/04 date
Daniel L. Stein	4/8/04 date

Final approval and acceptance of this dissertation is contingent upon the candidate's submission of the final copies of the dissertation to the Graduate College.

I hereby certify that I have read this dissertation prepared under my direction and recommend that it be accepted as fulfilling the dissertation requirement.

Dissertation Director: Koen Visscher 04/08/04 date

Statement by Author

This dissertation has been submitted in partial fulfillment of requirements for an advanced degree at The University of Arizona and is deposited in the University Library to be made available to borrowers under rules of the Library.

Brief quotations from this dissertation are allowable without special permission, provided that accurate acknowledgment of source is made. Requests for permission for extended quotation from or reproduction of this manuscript in whole or in part may be granted by the head of the major department or the Dean of the Graduate College when in his or her judgment the proposed use of the material is in the interests of scholarship. In all other instances, however, permission must be obtained from the author.

Signed: 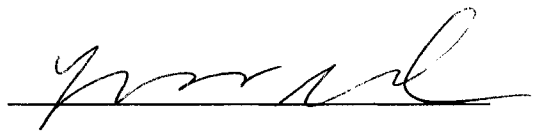

Acknowledgement

I want to show my gratitude to people whose guidance and support to make this possible.

First, I want to thank scientists whom I have collaborated with and without whom my achievement could not have been possible. Dr. Robert Maier taught me stochastic processes and helped me develop a theoretical insight which has become a valuable asset for an experimentalist to analyze one's experimental results. Dr. Daniel Stein guided me to perform the experiment with valuable discussion and support. I worked with Dr. Michael Brown to study solid state NMR. From him, I learned many important lessons to be a good scientist. I appreciate that he treats students with great respect and care. I feel grateful to Dr. Srinivas Mannes for being helpful on my exam committee and now my defense committee. Dr. Jose Garcia gave me a valuable advice when I made difficult decisions. Most of all, my advisor has been the most important person in my research. I feel grateful to his consistent support and help. He is a great experimentalist whom I always look up to. I should not forget my colleagues. I appreciate Chris Dombrowski and Joe Marotta for helping me write my thesis. I also want to thank Dr. Gary Skinner for sharing his creative ideas.

Last, I want to thank my family who always believe in me. I could never be thankful enough for their love and help.

Table of Contents

TABLE OF CONTENTS—*Continued*

List of Figures

LIST OF FIGURES—*Continued*

LIST OF FIGURES—*Continued*

LIST OF FIGURES—*Continued*

LIST OF FIGURES—*Continued*

LIST OF FIGURES—*Continued*

LIST OF FIGURES—*Continued*

List of Tables

Abstract

Our main research project is to develop an experimental system to understand the ribosomes as molecular motors. For this purpose, we designed and developed the single molecule ribosome motility assay. In this thesis, we discuss the related steps which we have taken to develop this assay: the instrumentation and four experiments. In the introduction, we illustrate the current experimental scheme and show the preliminary data of the single molecule ribosome translation.

In the first two chapters, we discuss two interesting experiments dealing with stochastic problems. In the first chapter, we introduce the idea that the noise can be reduced in certain conditions. We show that the noise can be really reduced but only if added fluctuations have to drive the input into states with reduced intrinsic noise. In the second chapter, we investigate two-state processes experimentally using a simple physical system in which a microscopic bead is trapped in a double-well potential. We discuss how we can control the characteristics of the escape process by adding a periodic force and illustrate the characteristics in terms of the residence time distribution and the escape phase. As last two chapters, we discuss the elastic and structural properties of homopolymeric RNA, polyadenylic acids (poly(A)), polycytidylic acids (poly(C)), and polyuridylic acids (poly(U)). First, we investigate the elastic property of poly(U) as a random coil. We find that the force-extension data is well predicted by a classic worm-like chain model at high Na^+ concentrations, whereas at low such concentrations the introduction of a scale-dependent persistence length is required. As single-stranded helices, poly(A) and poly(C) are studied. We stretch the molecules to induce the conformational transition from folded states to unfolded states and use the elastically coupled two-state model to acquire their structural information (about 9 bases per turn and 8 bases per turn, for poly(A) and poly(C) respectively, at neutral pH and 500 mM [Na^+]) and the free energy differences between two states (20 pN·nm

for poly(A) and 17.5 pN·nm for poly(C)).

Chapter 1

INTRODUCTION

The 'central dogma' of molecular biology introduced by Francis Crick [1] more than 40 years ago describes the flow of genetic information from DNA via RNA to protein, and constitutes a molecular synthesis sequence that is essential to life. Nature has provided a wide variety of specialized molecular machines that drive each step in this sequence. DNA polymerases, RNA polymerases and ribosomes are the engines driving DNA replication, RNA transcription and protein synthesis (translation), respectively [2]. In addition, there are molecules that manipulate or degrade DNA or RNA, such as helicases, topoisomerases, gyrases and nucleases [2]. Many of these molecules convert chemical energy into mechanical work and are able to move along their substrates (DNA or RNA). They can be viewed as molecular motors, in much the same way as the better known motor proteins myosin or kinesin. Years of research in biochemistry and structural biology have led to important insights about the mechanisms of these motor enzymes, but have provided limited understanding of how they work as molecular motors, and how chemistry and mechanics are coupled to produce enzyme movements. Single molecule techniques designed to probe the actions of individual motor molecules are now available to try to answer such questions. Atomic force microscopy, single molecule fluorescence microscopy, and optical tweezers have made it possible to image individual molecular motors and/or measure the displacements, velocities, and forces they produce [3–7]. In particular, optical tweezers have proven useful for studying molecular motors, because the forces they produce are of the same order of magnitude (pN) as those exerted by these enzymes. Using these techniques, the mechanical step sizes of individual myosin (~5 nm) [8] and kinesin (~8 nm) [9, 10] molecules have been measured. DNA polymerase, RNA

polymerase, and other enzymes using DNA or RNA as their templates also have been studied [3–5, 7]. On the other hand, the ribosome driven protein synthesis which links genotype and phenotype has not been paid much attention. The ribosome movement associated with the translation-elongation cycle might well be one of the most ancient and fundamental in biology, since ribosome structure and mechanism are so well conserved among all known forms of life. The main research focus in the laboratory is to probe these movements of a single ribosome along its mRNA template and to investigate how ribosomes work as molecular motors and protein-making machines.

In this introduction, we explain the biological background of ribosome directed protein synthesis and present the first preliminary data of ribosome movements. In addition, we illustrate the instrumentation specifically designed and developed for this purpose.

1.1 Principle of protein synthesis

During the process of protein synthesis, a ribosome carries out a number of intricate tasks. It facilitates the binding of factors (proteins) that initiate or terminate protein synthesis. In the elongation and translocation steps, it selects and binds transfer RNA (tRNA) carrying an amino acid in accordance with the codon sequence of messenger RNA (mRNA). It forms the peptide bonds, piecing together the amino acids that make up the protein. It subsequently moves the tRNA and associated mRNA, while maintaining the reading frame and ratcheting itself along mRNA molecule. Until a stop codon is reached, ribosome repeats this translocation and elongation step. A more detailed, but still oversimplified model of this translation-elongation cycle is illustrated in Fig. 1.1. In keeping with this complex set of tasks, the ribosome structure is equally complex. For example, the bacterial ribosome contains over 50 different proteins and 3 ribosomal RNA (rRNA) molecules with total length of more than 4500 nucleotides. These three rRNAs molecules make up more than half of

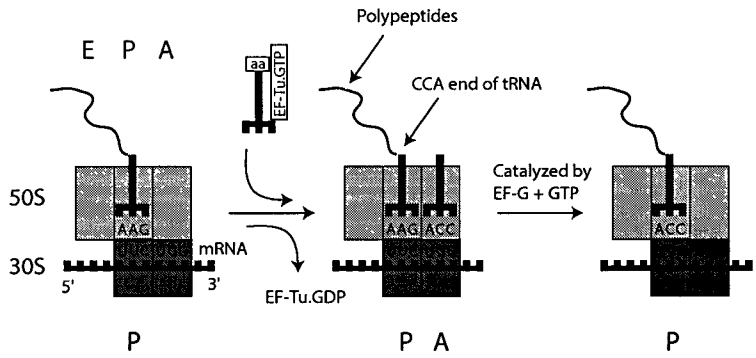

FIGURE 1.1. The translocation elongation cycle. The ribosome has 3 binding sites for tRNA, which are partitioned between the 30S and 50S subunits: an aminoacyl or A site; a peptidyl or P site; and the exit or E site. At the start of a cycle, a peptidyl tRNA carrying the polypeptide polymerized so far, is bound at the P site. Aminoacyl tRNA, which carries the next amino acid, is presented and binds at the A-site as a complex with elongation factor Tu (EF-Tu) and GTP. After codon recognition, GTP hydrolysis and dissociation of EF-Tu·GDP, the peptide bond is formed, which results in a peptidyl tRNA in the A-site and a deacylated tRNA in the P-site. The subsequent translocation step is catalyzed by another GTPase, elongation factor G (EF-G), and completes the cycle by moving peptidyl tRNA to the P site, and deacylated tRNA to the E site. During the translocation step, the mRNA is carried along by its associated tRNA, thereby effectively 'ratcheting' the ribosome into 5' to 3' direction along the mRNA molecule.

the weight of the ribosome, ~2.5 MDa. Bacterial ribosomes have two distinct and recognizable subunits: a small 30S and a large 50S (eukaryotic ribosomes are a little more complex and heavier, composed of a 40S small and a 60S large subunits). The 30S subunit essentially binds mRNA and the anti-codon end of tRNA, while 50S subunit interacts with the CCA-end of tRNA and catalyzes peptide bond formation. The kinetics of the translocation-elongation cycle has been elucidated by steady-state and transient kinetics studies [11]. However, due to the complexity of its structure and mechanism, it is not clear which of many components or associated factors make up the motor or engine driving the translocation step. Several models have been proposed to describe these complex steps, and yet they are still short of describing the complete picture of the translocation and elongation process [12–14]. Single-

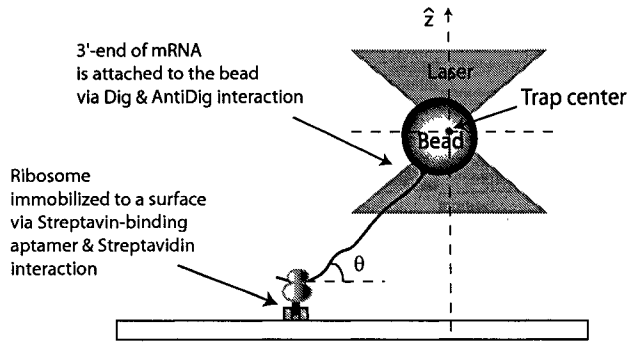

FIGURE 1.2. The geometry of the ribosome single molecule assay: the 5'-end of mRNA is tethered to the ribosome immobilized on the surface and its 3'-end is attached to the optically trapped polystyrene bead. θ specifies the angle between mRNA and the surface.

molecule techniques have been used to measure directly the elementary events of production of force and displacement by molecular motors [3, 6, 7, 15–17], helping to elucidate their properties and mechanisms. Since the movement of the ribosome along the mRNA template utilizes the similar mechanochemical properties, we believe that the single-molecule measurements will provide valuable information toward the understanding of the translocation and elongation in protein synthesis.

1.2 Single-molecule motility assay

To study protein synthesis at the single molecule scale, a new biochemical *in vitro* assay as well as new instrumentation needed to be developed. The purpose of the biochemical *in vitro* assay is to create an experimental environment or geometry in which the relevant physical quantities can be measured accurately while assuring the ribosome's functionality and translational rate remain close to those *in vivo*: $10 \sim 20$ peptide bonds/s at 37°C (this biochemical assay has been developed by Dr. Gary Skinner, a postdoctoral researcher in our lab). In Fig. 1.2, the single molecule experimental scheme is illustrated. Ribosome motion is determined by measuring the position of a microscopic bead attached to the mRNA molecule being drawn in by a

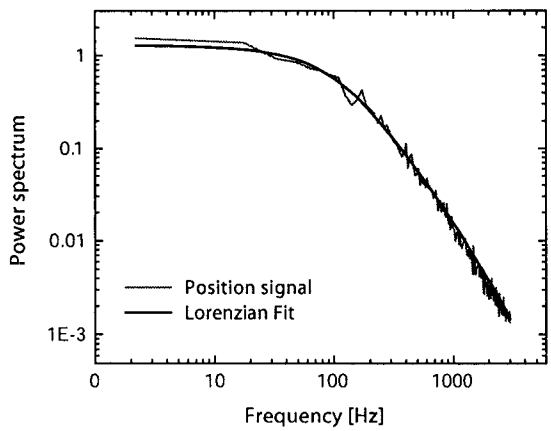

FIGURE 1.3. Power spectrum of the position signal. One way to measure the stiffness of the trap is to fit the power spectrum with Lorenzian fit and acquire the roll-off frequency.

surface-immobilized ribosome. The ribosome should be immobilized on the surface in order to apply a force or to measure the force produced by the molecule. This can in principle be achieved with either non-specific binding of a ribosome or attaching it specifically using known ligand interactions by modifying the surface and the ribosome. Since the ribosome functionality is highly coupled to its conformational change, the non-specific binding scheme where any parts of ribosomes can stick to the surface may hinder the ribosome movement. Therefore, we modified ribosomes to include a streptavidin-binding aptamer which enables immobilization by a short (~30 nm) polyethylene glycol (PEG) molecule. In addition, the 3'-end of mRNA has been modified to have digoxigenin which binds to an anti-digoxigenin coated polystyrene bead. Since we can neither observe nor manipulate the individual biological molecules directly (including ribosomes and RNA), we attach these to small dielectric particles (silica or polystyrene beads (diameter 250 nm $\sim$ 2 μm)) and manipulate the molecules indirectly by trapping these beads using optical tweezers (Fig. 1.2).

Simultaneously with the development of the biochemical *in vitro* motility assay, we have built a feedback controlled optical tweezers for translation and force measurements. The optical tweezers is a single-beam laser trap for dielectric particles created

by focusing a laser beam to a diffraction limited spot using a large numerical aperture microscope objective [18]. When the focused laser beam passes through a silica or polystyrene bead, it generates not only a scattering force but also a gradient force. Since the laser beam induces electric dipoles, the bead experiences a time-averaged force toward high intensity regions (the focal spot). This gradient force brings the bead into the focal point, while the scattering force pushes the bead away from the focal point. Thus, the trapping is possible only if the gradient force is larger than the scattering force. In order to create the intense field gradient near the focal region, high numerical aperture microscope objective is required [18, 19]. The precise trapping force experienced by the bead is difficult to be quantified using theoretical calculations. However, they are readily measured experimentally once appropriate calibrations have been done. It has been empirically shown that the optical force increases linearly for small displacements out of the focal point (~200 nm) and thus, the trap behaves as a spring. The force can then be calculated by multiplying the trap spring constant and the displacement of the particle from the trap center. The trap spring constant (trap stiffness) can be calibrated using a variety of methods, with two used here: the power spectrum and equipartition theorem methods. These two methods are based on the stochastic properties of the bead's motion in the trap. The equation of motion of a bead in an optical trap follows the Langevin equation for the overdamped case (consider one dimension for simplicity),

$$\alpha\dot{x} = -kx + c\xi(t). \tag{1.1}$$

Here k indicates the stiffness of the trap, α is a drag coefficient given by $6\pi\eta r$ where η is the viscosity of the medium and r is the radius of the bead. $\xi(t)$ represents the typical white noise with strength c. The power spectrum is readily calculated by taking a fourier transform of Eq. 1.1,

$$|X(f)|^2 = \frac{c^2}{k^2 + (2\pi\alpha f)^2}. \tag{1.2}$$

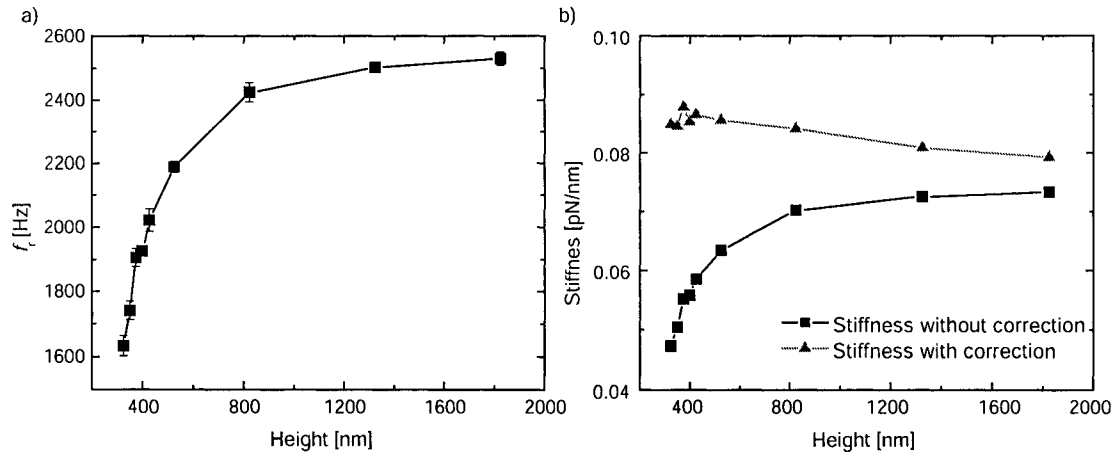

FIGURE 1.4. Height dependent roll-off frequency, f_r. a) Due to the hydro-drag effect, the measured roll-off frequency of the trapped bead is dependent on the height from the surface. In order to acquire the correct stiffness from f_r, the hydro-drag effect should be corrected using the Faxen's law (Eq. 1.3). b) The stiffness with correction is relatively constant over height.

In the frequency domain, the amplitude, $|X(f)|^2$ is cut off at a frequency, defined as a roll-off frequency, f_r=$k/(2\pi\alpha)$. Experimentally, the roll-off frequency is readily obtained by fitting a Lorenzian to the power spectrum of the trapped bead position (Fig. 1.3). In general, the power spectrum method is useful to identify any undesired noise sources with distinct frequency signatures. The roll-off frequency is dependent on the viscous drag coefficient and thus on the height of the trapped bead above the surface, h (Fig 1.4[a]). Therefore, it is advised to use this method either by putting the bead sufficiently far away from the surface ($h > 2r$) or by precisely measuring the height of the bead and applying a correction to the viscosity using the Faxen's law as follows (Fig. 1.4[b]) [19],

$$\eta' = \frac{\eta}{1 - \frac{9}{16}\left(\frac{r}{h}\right) + \frac{1}{8}\left(\frac{r}{h}\right)^3 - \frac{45}{256}\left(\frac{r}{h}\right)^4 - \frac{1}{16}\left(\frac{r}{h}\right)^5}. \tag{1.3}$$

η' replaces η in the f_r to correct the change of the drag effect in terms of the height, h.

Since the optical trap behaves as a harmonic potential within certain range of bead

displacements ($\sim \pm 200$ nm), we can also use the equipartition theorem to determine the trap stiffness:

$$\frac{1}{2}k_BT = \frac{1}{2}k\langle x^2 \rangle. \tag{1.4}$$

The stiffness measured using two methods are in agreement within 10% absolute error for low to moderate stiffness (0.005 pN/nm $< k_b <$ 0.1 pN/nm). However they deviate up to 30% when the stiffness becomes high ($>$ 0.1 pN/nm), which is largely due to the difficulty in fitting the power spectrum when f_r becomes large.

The instrument is capable of measuring nm-sized displacements and pN-scaled forces produced by a single molecule. Such measurements require the reduction of mechanical drifts and vibrations. Hence the entire optical instrument has been built on the vibration-isolated table (Newport) in an acoustic-isolated and temperature-controlled room. The optical instrument consists of optical tweezers and the position detection system, which are further integrated into the microscope (Fig. 1.5). Lasers used for the optical trapping are required to be in the wavelength region of 800 $\sim$ 1100 nm to minimize photo-damage and water-heating [19, 20]. Water absorbs light increasingly farther into the infrared [19]. Therefore, we use a 1064 nm CW laser (Spectra Physics) for optical trapping. The diameter of the laser beam is magnified with two beam expanders (BE and TL1 & TL2) to slightly overfill the back aperture of the objective (Fig. 1.5). In addition, for computer control of the position and intensity of the optical trap, we place acousto-optic deflectors (AODs, IntraAction Corp) in the laser beam path. AODs utilize density gratings formed by traveling acoustic wave in a crystal. When a laser beam comes across the crystal, it diffracts at the density wave. The Bragg angle θ of the first diffracted order is controlled by computer using a frequency synthesizer as it is given by $\lambda f/v$ where λ is the wavelength of the light, f and v are the acoustic wave frequency and velocity, respectively. Manual control of the trap position is achieved by moving a lens (TD/L).

For precise positioning of the specimen, we mounted a computer-controlled, high-

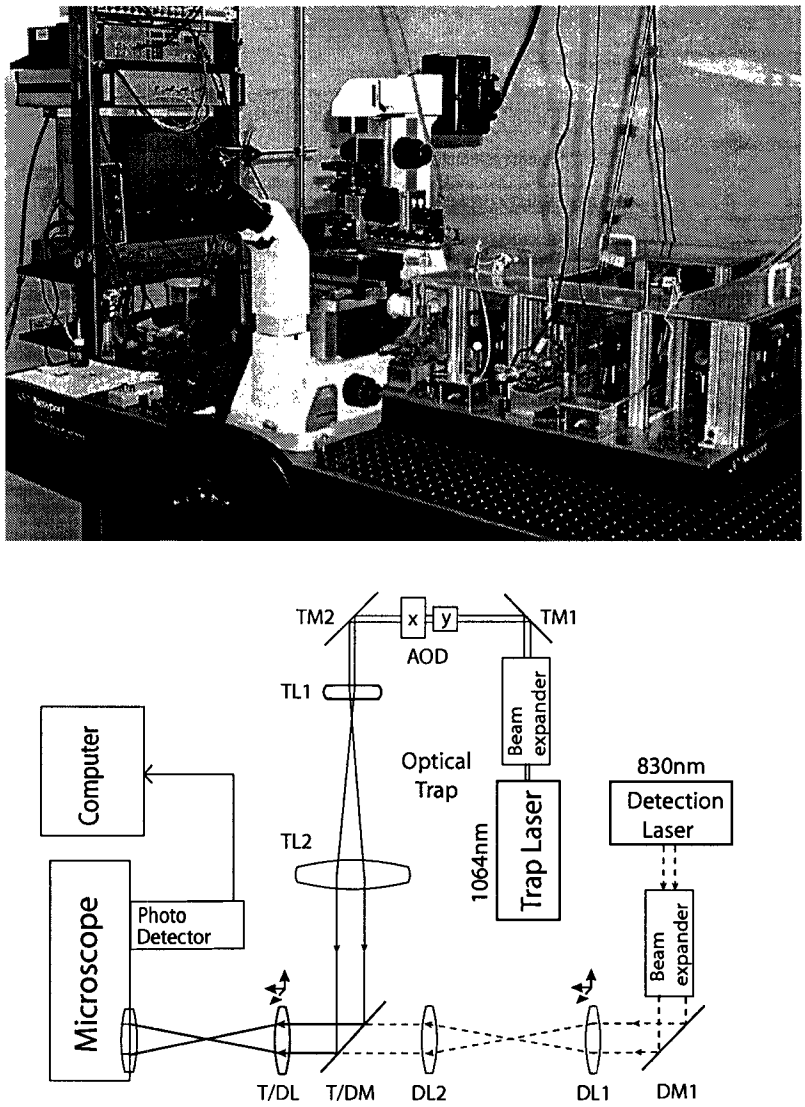

FIGURE 1.5. Experimental set-up: For the optical trap, TM1 and TM2 are two mirrors guiding the laser beam into acousto-optic deflectors (AODs) which are used for modulating the position and intensity of the laser trap and into the microscope. TL1 and TL2 are two lenses (f=10 and 30 cm respectively) working as a beam expander, at the same time imaging AODs onto the movable lens TD/L. T/DM is a dichroic mirror combining the trapping laser light and the detection laser light. T/DL is a movable lens to manually control the positions of both laser spots at the specimen plane, and is imaged onto the back aperture of the microscope objective. The optical components for the position detection consist of DM1, DL1, and DL2, indicating a mirror, a movable lens (f=6.5 cm) which controls the detection laser spot at the specimen plane, and a fixed lens (f=6.5 cm), respectively. The position signal of the trapped bead from the photo-detector is transferred to the computer.

resolution piezo-driven XYZ stage on a manually operated microscope stage. With this device, the position of the specimen can be controlled by computer in increments as small as 1 nm over 100 x 100 μm. In addition to the x and y positioning, its capability to move into the z-direction (i.e. along the optical axis) at high resolution enables us to accurately locate the cover glass surface of the specimen ($\sim$10 nm resolution) with respect to the trapped bead. Thus, the experimental geometry (the angle of mRNA relative to the surface) is well specified (Fig. 1.2).

To determine the displacement of the particle from the trap center, the change in the direction of a second laser beam focused onto the particle and scattered or deflected due to bead motion is measured by collecting this forward scattered laser light and projecting it onto a quadrant photodiode. In principle, the optical tweezers can be used as a laser source for such a position detector, but the use of an additional focused laser beam, which has been overlapped with the optical tweezers has an advantage: it enables on-the-fly calibration of the position detector. Using one-time calibrated AODs, one can move the trapped bead over a known distance through the laser spot of the position detector while the signal from photodiode is further amplified and digitized using the anti-aliasing filter and transferred to the computer. Thus, on-line fitting procedure readily produces the detector response in nm/volt.

1.3 Preliminary results of single molecule ribosome assay

In the single molecule assay, we use a force-clamp method where a constant force is applied to a molecule using a computer-controlled feedback loop. Since the ribosome is immobilized to the surface, the mRNA will be drawn through the ribosome and the tethered bead will be pulled out of the center of the fixed optical tweezers during the translocation (Fig. 1.2). Without a force-clamp, this displacement will be simply measured and the optical forces exerted can be calculated using the calibrated stiffness of the optical tweezers. When we use a force-clamp, as soon as the bead displaces

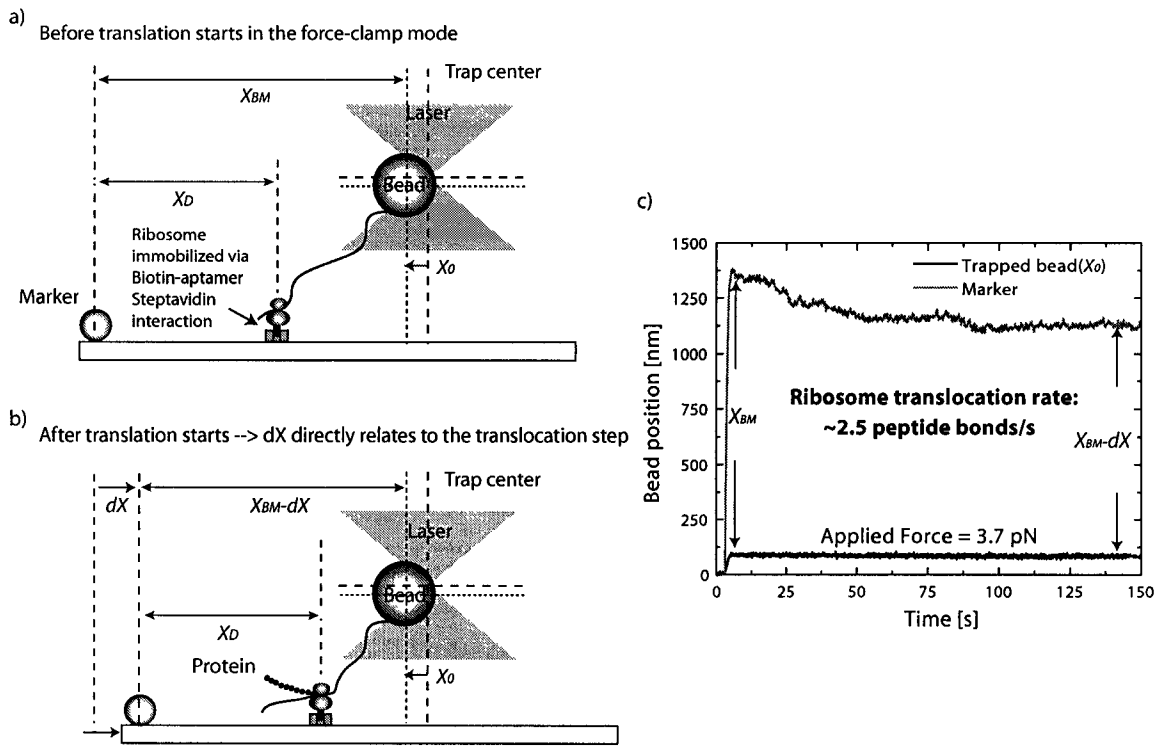

FIGURE 1.6. The ribosome motility assay using a force-clamp. The ribosome is immobilized via the streptavidin-binding aptamer and streptavidin. a) Once the force-clamp mode starts, the piezo-stage moves until the trapped bead position reaches the set position, X_0 (set force). Before the proper buffer containing necessary substrates for translation are introduced, the tether length remains the same and the piezo-stage does not move except for correcting stage drift. b) Once the ribosome starts translation, the tether length will get shorter, the bead will be pulled out of the initial position. Simultaneously, the force-clamp moves the stage to the right by the amount of dX to maintain X_0. In this set-up, the distance between the trapped bead and the marker (X_{BM}) will be constant as long as the tether length does not change. Hence even if there is stage drift causing the trapped bead to be pulled away from the set position, X_{BM} will be constant and dX is zero. dX is directly related to the change of the tether length which only occurs through the ribosome and the mRNA interactions. c) Video-tracking of two beads shows that there is a shortening of the tether. Based on dX, the translation rate is calculated as 2.5 peptide bonds/s.

from the initial set point relative to the center of the trap, the feedback controlled force-clamp kicks in and changes the ribosome position by controlling the piezo-stage until the bead has returned to the initial position. Hence the applied force will remain constant during the experiment. One big advantage of this force-clamp is that we can easily convert the stage movement into the ribosome translocation rate. According to our studies on the elastic properties of homopolymeric RNA (discussed in chapter 4 and 5), poly(U) which is used as mRNA is well described by a worm-like chain model and thus, the relative extension of the molecule can be expressed as,

$$\frac{x}{L} = 1 - \frac{1}{2\sqrt{F_s L_p / k_B T + 1/4}} = constant. \tag{1.5}$$

Here x/L is the relative extension of the molecule at the set force, F_s. For a given force F_s, the relative extension remains a constant and the change of the contour length of the molecule is obtained by dividing the stage movement by the relative extension. Combined with the force-clamp method, we introduce the following scheme such that the bead displacement will be insensitive to possible stage drifts. As illustrated in Fig. 1.6, we attach a marker bead on the surface. The distance between the marker bead and the trapped bead will be used as the signal since it is not affected by stage drift. If the length of the tethered mRNA changes, the distance between the two beads, which is identified by video-tracking, will also change (Fig. 1.6^c). Because the change in the stage position is directly proportional to the change in contour length (Eq. 1.5), velocities and thus translation rates can be determined. For example, as shown in Fig. 1.6^c, the set force is 3.7 pN and the calculated x/L is 0.54 (L_p ~1 nm) so that the translation rate is calculated as ~ 2.5 peptide bonds/s where one codon (spans 3 nucleotides) corresponds to 1.74 nm. In fact, it is close to that measured in *in vitro* translation assays performed in the test tube. Furthermore, this kind of movement has not been observed in the absence of elongation factors known to be required for ribosome translation.

1.4 Dissertation contents

This dissertation consists of experiments that I have performed using optical tweezers. These also served a second purpose in that they enabled the careful testing in calibration of the experimental set-up used for the single molecule ribosome assay. In chapter 1, we performed an experiment to verify the theoretically predicted reduction of noise observed at the output of a physical system by introducing extra noise at its input. In chapter 2, we studied "physically" simple two-state reaction kinetics based on the Kramers theory to understand how this reaction kinetics depends on external force using two optical traps. Many biological and chemical processes can be described by a two-state model such as protein folding/unfolding, ligand binding, and RNA folding/unfolding (Chapter 5). This study shows how external force can direct these reaction processes. It also gives us an insight in a simple picture of how a molecular motor could move along a (periodic) potential and how this system (motor in a potential) would react to external force. In chapter 3 and 4, we will discuss the elastic and structural properties of homopolymeric RNA. These two topics are more directly related to the ribosome project because knowledge of the elastic properties (persistence length) is essential to derive ribosome properties from bead position measurements.

Chapter 2

NOISE REDUCTION BY NOISE

It has been theoretically demonstrated that noise can be used to suppress noise [21, 22]. Here we investigate this phenomenon experimentally using a model system consisting of a 'Brownian' bead held in an optical trap whose position and stiffness fluctuate. First, we identified two measures of noises of this system: the signal variance and the variance of the estimation of the mean. Secondly, we verified that both of noises could be effectively suppressed according to the theoretical predictions. We found that the critical property for noise suppression is that added fluctuations have to drive the input into the states with reduced intrinsic noise.

2.1 Introduction

Although noise is generally considered a nuisance, its constructive properties have become increasingly clear as it plays essential roles in many fundamental processes, particularly in biology. For example, mechanochemical reactions by motor proteins requires the presence of thermal fluctuations [23, 24]. Furthermore, the response of sensory systems can be maximized by cooperative interactions between noise and an external driving signal [25] - a phenomenon known as stochastic resonance [26, 27].

Another beneficial aspect of noise has come to light: noise may be used to reduce noise [21]. The concept of noise-suppression-by-noise was originally proposed by Vilar and Rubí [21]. They suggested that the noise observed at the output of an intrinsically noisy system might be suppressed by adding noise at its input. In addition, they provided perturbation formulas for the effective mean response and a measure of the intensity of noise. However, it was implicated that the reduction in the effective output noise might be largely dependent on the scale of fluctuations in the underlying

state and the auto correlation time of the state.

Recently, it has been clarified [22] that the measure of noise discussed by Vilar and Rubí is actually an asymptotic variance of the estimation error of the mean rather than the signal variance. It further demonstrated that the signal variance might be also reduced by the input noise independent of the auto correlation time of the states. In particular, it provided a simple way to measure both noises (the signal variance as well as the variance of the estimation error) using power spectrum analysis [22]. First, we outline the mathematical framework of a system and variables of interest following the theoretical work by Walton et.al [22] and describe how we adapt this work to our experiment to determine the conditions under which noise can be reduced. Afterwards, we verify the idea "noise-suppression-by noise" experimentally using an optically trapped Brownian bead in water.

2.2 Mathematical framework

The system under consideration essentially models an observed signal that is regulated by an underlying state, X. The output signal, Y, will be the noisy observation at the output. Heuristically, we can write

$$Y(t) = H(X(t)) + \xi(X(t), t), \tag{2.1}$$

where the function H gives the mean response and ξ is a state-dependent noise process. Note that Y fluctuates due to the randomly changing state X as well as to the intrinsic noise ξ. The noise process, ξ will be white-Gaussian, have zero mean $\langle \xi(X(t), t) \rangle = 0$ (averages will be notated as angled brackets ($\langle \cdot \rangle$)), with an amplitude that depends on the state, X:

$$\langle \xi(X(t), t) \xi(X(s), s) \rangle' = G(X(t)) \delta(t - s), \tag{2.2}$$

where the superscript on the angled brackets denotes averaging over the intrinsic noise but not over the fluctuating state. Consequently, we also have

$$\langle Y(t)\rangle' = H(X(t)). \tag{2.3}$$

On the other hand, the underlying state X is modeled as a stationary Gaussian process with mean x_0, variance σ^2, and an autocorrelation that decays exponentially with a relaxation time τ_X,

$$\gamma_X(u) = \langle \widetilde{X}_t \, \widetilde{X}_{t+u} \rangle = \sigma^2 e^{-|u|/\tau_X}, \tag{2.4}$$

where $\widetilde{X} = X - X_0$ is the centered process which measures the difference between the state X and its mean.

For the discrete case, we can establish formulas analogous to Eqs. (2.1) and (2.4). We introduce an independent and identically distributed sequence of Gaussian random variables $\{\varepsilon_k\}$, each with zero mean and unit variance and independent of X, so that

$$Y_k = H(X_k) + \beta(X_k)\varepsilon_k, \tag{2.5}$$

where $\beta^2(X)$ is analogous to the function $G(X)$ in Eq. 2.2. Similarly, an autocorrelation of X can be expressed,

$$\gamma_X(p) = \langle \widetilde{X}_k \, \widetilde{X}_{k+p} \rangle = \sigma^2 \rho^{|p|}. \tag{2.6}$$

Here, ρ is an autocorrelation constant, replacing $e^{-|u|/\tau_X}$. We remark that in the discrete case, if observations are sampled every nth step, $Y_k^* = Y_{nk}$, the resulting system is equivalent to the system already described, except that the corresponding state sequence $X_k^* = X_{nk}$ has autocorrelation $\rho^* = \rho^n$.

First, we compute the asymptotic mean response of the underlying state, X. Because the state process X_t is stationary, the mean signal output or mean response

H_0, which depends on X_0 and σ, will simply be the stationary average of $H(X_t)$,

$$H_0 \equiv \langle Y_t \rangle = \langle H(X_t) \rangle \tag{2.7}$$

$$= \int_{-\infty}^{\infty} H(x)\phi(x; x_0, \sigma^2)dx, \tag{2.8}$$

where $\phi(x; x_0, \sigma^2)$ is a Gaussian density with mean x_0 and variance σ^2

$$\phi(x; \mu, \eta^2) = \frac{1}{\sqrt{2\pi\sigma^2}} \exp\left(-\frac{(x - x_0)^2}{2\sigma^2}\right). \tag{2.9}$$

Note that because of the stationarity of X, the time t is arbitrary. The same calculation also applies in the case of discrete time. Given this asymptotic mean response, we define the centered response $\widetilde{H}(X) = H(X) - H_0$.

Bases on these, we can define two measures of output noises. First, we start with the signal variance, S_0^2. Under the stated assumption that the intrinsic noise is a white noise, S_0^2 will only be defined in the case of discrete time. Because the intrinsic noise ξ has zero mean independent of the state, we find that for the discrete time case,

$$S_0^2 \equiv \langle [Y_k - H_0]^2 \rangle = \langle \langle [\widetilde{H}(X_k) + \beta(X_k)\varepsilon_k]^2 \rangle' \rangle \tag{2.10}$$

$$= \langle \widetilde{H}^2(X_k) \rangle + \langle \beta^2(X_k) \rangle. \tag{2.11}$$

Consequently, the signal variance is composed of two parts. The first contribution, $\langle \widetilde{H}^2(X_k) \rangle$, represents the variability arising from fluctuations in the mean response because the state itself is changing. The second contribution, $\langle \beta^2(X_k) \rangle$, represents the average scale of additional intrinsic noise which comes from a noisy input. When the input state does not fluctuate, in that $\sigma = 0$, the variance $\langle \widetilde{H}^2(X_k) \rangle$ will necessarily vanish since the mean response $H(X)$ will be constant. However, when $\sigma > 0$, this variance will be strictly positive unless H does not depend on the state but is constant. Therefore, the overall signal variance S_0^2 can decrease only if the average of the intrinsic noise decreases, $\langle \beta^2(X_k) \rangle < \beta^2(x_0)$. Furthermore, the additional fluctuation in the signal due to the non-constant response, $\langle \widetilde{H}^2(X_k) \rangle$ must remain

sufficiently small so as not to negate the effect.

Next, the second type of output noise is the asymptotic variance of the estimation error, β_0^2 given by,

$$\begin{aligned} \beta_0^2 &\equiv \lim_{n\to\infty} n\langle(\overline{Y}_n - H_0)^2\rangle && (2.12)\\ &= \sum_{p=-\infty}^{\infty} \langle(Y_k - H_0)(Y_{k+p} - H_0)\rangle && (2.13)\\ &= \sum_{p=-\infty}^{\infty} \langle\widetilde{H}(X_k)\widetilde{H}(X_{k+p})\rangle + \langle\beta^2(X_k)\rangle, && (2.14) \end{aligned}$$

where $\overline{Y}_n$ indicates a running average of the output signal. Similar to the signal variance S_0^2, the resulting asymptotic variance of the estimation error β_0^2 has two contributions shown in Eq. 2.14. Although both forms of asymptotic noise involve the stationary average $\langle\beta^2(X_k)\rangle$, the variance β_0^2 involves the sum of all autocovariances of the centered process $\widetilde{H}(X_k)$ rather than just the variance, as occurs for S_0^2.

We remark that both variances also relates to the power spectrum [22]. For the discrete autocovariance of the output Y_k,

$$\gamma_Y(p) = \langle(Y_k - H_0)(Y_{k+p} - H_0)\rangle, \tag{2.15}$$

we define the spectral density $h(\omega)$ as the Fourier series,

$$h(\omega) = \frac{1}{2\pi}\sum_{p=-\infty}^{\infty} \gamma_Y(p)e^{-i\omega p}, \tag{2.16}$$

defined over the interval $[-\pi, \pi)$. The autocovariance function can be recovered from the spectral density as

$$\gamma_Y(p) = \int_{-\pi}^{\pi} h(\omega)e^{i\omega p}d\omega. \tag{2.17}$$

Consequently, we have that the signal variance corresponds to the total spectral power of the output signal,

$$S_0^2 = \gamma_Y(0) = \int_{-\pi}^{\pi} h(\omega)d\omega. \tag{2.18}$$

When the state X does not fluctuate, the spectral density has a constant height of $h(\omega) = \beta^2(x_0)/2\pi$. So for the signal variance to decrease, the power spectral density must, on average, lie below this level. β_0^2 becomes simply $2\pi h(0)$ since it is the sum of all autocovariances of the process Y as defined in Eq. 2.13.

Experimentally, the determination of β_0^2 is most easily accomplished by estimating the power spectral density and then determining the density at zero frequency. A natural estimator of the spectral density is the periodogram of the observation sequence [28], which corresponds to the squared-amplitude of the discrete Fourier transform of the observed sequence. Unfortunately, the periodogram has persistent fluctuations due to the stochastic nature of the observation sequence. To decrease the variance of the estimate of the spectral density, one can average the periodogram over a relatively small bandwidth but with the introduction of some bias in the estimate [28]. In principle, if one had many parallel observation sequences, one could also compute the variance of the ensemble of sample means and then estimate the asymptotic variance directly. It is critical to note that the variance of the estimation error β_0^2 involves an autocorrelation time as a multiplicative factor times the variance of H, but that S_0^2 only involves the variance of H. The essential difference is that the signal noise S_0^2 represents the variation in the signal as the process X ergodically samples its phase space, whereas the estimation errors β_0^2 represent an accumulated bias in the estimate $\overline{Y}$.

2.3 Experimental application

The experiment is designed to follow the theoretical model system described in the previous section. As a reminder, it is a intrinsically noisy system with an externally controlled variable. An intrinsically fluctuating system is readily accessible by using a microscopic silica bead held in an optical trap. For our purposes, the position of the optical trap and a bead take the role of the input state, X_k, and output or observation,

Y_k, respectively. At each position of the trap the bead fluctuates with a variance, $\beta^2(X_k)$, inversely proportional to the stiffness of the trap, $k(X_k)$, representing the state-dependent intrinsic noise. We externally manipulate the position of the trap to implement the required statistical properties of the input state. Furthermore, the trap stiffness is varied upon the trap position relative to its means position, a necessary requirement to achieve noise-reduction.

The output Y_k will be a noisy function of the input state X_k, given by

$$Y_k = H(X_k) + \beta(X_k)\epsilon_k, \tag{2.19}$$

with $H(x_k)$ the mean response, ϵ_k a sequence of Gaussian random variables with zero mean and unit variance. Input noise is added by moving the trap in a stochastic fashion,

$$X_{k+1} = \rho X_k + \frac{\sigma}{\sqrt{1-\rho^2}}\zeta_{k+1}, \tag{2.20}$$

where ζ_k is a sequence of independent, standard normal random variables, σ the variance of trap positions, and ρ the autocorrelation [22]. Because observations of the position of a trapped bead represent unbiased estimates of the trap position itself, the mean response simply becomes $H(X_k) = X_k$.

Next we need to specify the 'noise response' or the state-dependence of the intrinsic noise $\beta^2(X_k)$. We require that, at least for some values of X_k, $\beta^2(X_k)$ decreases below the base value of $\beta^2(0)$. For ease in computation we choose the function

$$\beta^2(X) = \begin{cases} (\beta_1 + m_+ x)^2 + \beta_2^2 & \text{if } X > 0, \\ (\beta_1 + m_- x)^2 + \beta_2^2 & \text{if } X < 0. \end{cases} \tag{2.21}$$

The parameters m_+ and m_- control how steeply the noise varies as the trap departs from its mean position. Thus, the minimum possible variance is β_2^2, bounded by the maximum trap stiffness, $k_{\max} = k_B T/\beta_2^2$.

Using the power spectrum analysis [22], we compute the power spectrum of the output signal as ,

$$h(\omega) = \frac{1}{2\pi}[\frac{1}{2}\sigma^2 m^2 + \sqrt{\frac{2}{\pi}}\beta_1\sigma\Delta m + \beta_1^2 + \beta_2^2 - \frac{2}{\pi}\beta_1^2 + \frac{(1-\rho^2)\sigma^2}{1+\rho^2-2\rho\cos\omega}], \tag{2.22}$$

with m^2 and Δm defined as

$$m^2 = m_+^2 + m_-^2, \tag{2.23}$$

$$\Delta m = m_+ - m_-. \tag{2.24}$$

One thing we should note that ρ in the output observation is not the same as ρ in Eq. 2.20. ρ in the output observation is dependent on the ratio of the sampling time to the trap movement time. For example, if we sample the bead position every other the trap movement, ρ in the output observation is the square of ρ in Eq. 2.20.

The asymptotic variance of the estimate errors of the mean, ${\beta_0}^2 = 2\pi h(0)$ follows readily from Eq. 2.22

$$\beta_0^2 = \beta^2(0) + \sigma^2(\frac{1}{2}m^2 + \frac{1+\rho}{1-\rho}) + \sqrt{\frac{2}{\pi}}\beta_1\sigma\Delta m. \tag{2.25}$$

as does the signal variance S_0^2,

$$S_0^2 = \beta^2(0) + \sigma^2(\frac{1}{2}m^2 + 1) + \sqrt{\frac{2}{\pi}}\beta_1\sigma\Delta m, \tag{2.26}$$

It is important to note that this analysis is valid for any size σ^2. In fact, the perturbation technique used by Vilar and Rubí would break down in our case because $\beta^2(X)$ is not differentiable at $X = 0$.

The signal variance can be shown to fall below the baseline level (when $\sigma^2 = 0$) whenever m_+ and m_- lie on a disk in (m_+, m_-)-parameter space,

$$(m_+ + \sqrt{\frac{2}{\pi}}\frac{\beta_1}{\sigma})^2 + (m_- - \sqrt{\frac{2}{\pi}}\frac{\beta_1}{\sigma})^2 < \frac{4}{\pi}\frac{\beta_1^2}{\sigma^2} - 2. \tag{2.27}$$

and $\sigma^2 < \frac{2\beta_1^2}{\pi}$. Similarly, the asymptotic estimation error β_0^2 is reduced inside a smaller disk with the same center,

$$(m_+ + \sqrt{\frac{2}{\pi}}\frac{\beta_1}{\sigma})^2 + (m_- - \sqrt{\frac{2}{\pi}}\frac{\beta_1}{\sigma})^2 < \frac{4}{\pi}\frac{\beta_1^2}{\sigma^2} - 2\frac{1+\rho}{1-\rho}, \tag{2.28}$$

and a decrease only occurs for $\sigma^2 < \frac{2\beta_1^2}{\pi}\frac{1-\rho}{1+\rho}$. In both cases, fluctuations in the input state drive the intrinsic noise into states with smaller noise scales, leading to a

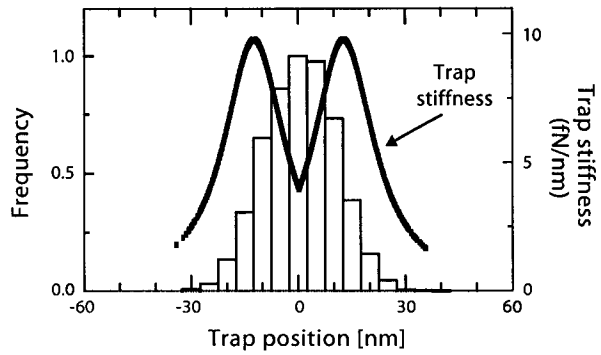

FIGURE 2.1. Quantitative description of fluctuating input state. To introduce external fluctuation at the input, the trap is controlled to move following a random Gaussian distribution. The characteristics of the trap displacement is visualized by plotting the histogram of trap positions. Solid line indicates the trap stiffness related to the trap position.

decrease in $\langle \beta^2(X_k) \rangle$.

To maximize the suppression of noise in our experiments, we select (m_+, m_-) (for each level of noise σ^2) corresponding to the center of the disks,

$$m_+ = -\sqrt{\frac{2}{\pi}}\frac{\beta_1}{\sigma}, \quad \text{and} \quad m_- = \sqrt{\frac{2}{\pi}}\frac{\beta_1}{\sigma}. \tag{2.29}$$

As a result in our experiments, the stiffness of the trap increases symmetrically to a maximum stiffness at $|X| = \sigma\sqrt{\pi/2}$, beyond which the stiffness continually weakens (see Fig. 2.1). With these conditions the power spectral density, and the noise measures have simple expressions,

$$h(\omega) = \frac{1}{2\pi}[\beta_1^2 + \beta_2^2 - \frac{2}{\pi}\beta_1^2 + \frac{(1-\rho^2)\sigma^2}{1+\rho^2-2\rho\cos\omega}] \tag{2.30}$$

$$S_0^2 = \beta_1^2 + \beta_2^2 - \frac{2}{\pi}\beta_1^2 + \sigma^2 \tag{2.31}$$

$$\beta_0^2 = \beta_1^2 + \beta_2^2 - \frac{2}{\pi}\beta_1^2 + \sigma^2\frac{1+\rho}{1-\rho}. \tag{2.32}$$

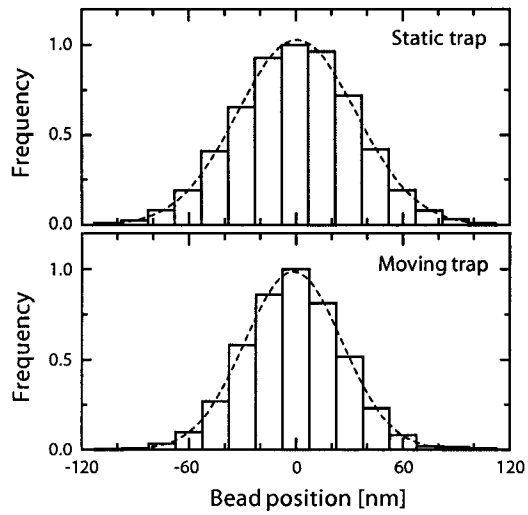

FIGURE 2.2. Suppression of noise illustrated by the reduction of the mean squared displacement. The difference of the signal variance between two conditions is clearly noticeable when the bead position histograms are compared. Upper figure indicates the bead position histogram in a non-moving trap. The bottom figure is the histogram for the condition when the trap is moved stochastically with $\sigma = 5$ nm. Dotted line indicates Gaussian fit to illustrate the characteristic of the bead position.

2.4 Experimentation

The optical trap used in this experiment has been previously described [29]. However, briefly, the beam of a Nd:YVO_4 laser (wavelength 1064 nm) is passed through two acousto-optical deflectors to control trap position as well as stiffness, and focused down to a diffraction limited spot using a microscope objective to form the optical trap. A second laser beam (wavelength 830 nm), is overlapped with the trap to measure the bead position by analyzing deflections of forwarded scattered laser light using a quadrant photodiode. The power of this laser is kept to a minimum so as not to exert any discernible force on the bead. Detector signals are amplified, anti-alias filtered, digitized and stored by computer. For further details see Visscher et al. [29]. A 0.64 μm diameter silica bead (Bangs Labs) was trapped in water. The baseline stiffness of the trap was $k(0) = 3.73 \pm 0.09$ fN/nm (mean±s.e.m, N=3), determined from the mean squared displacement of the bead, and in agreement with the value

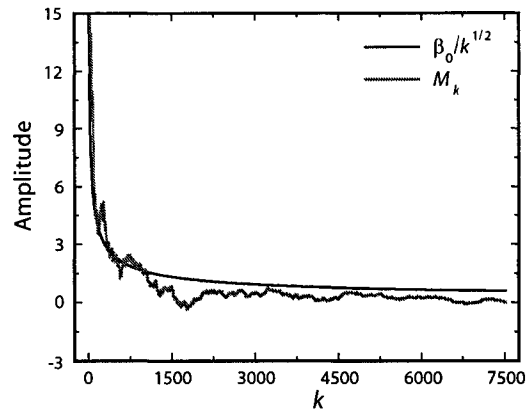

FIGURE 2.3. Interpretation of β_0 in terms of running average, M_k. Although β_0 cannot be directly measured in the time domain, the general tendency can be understood by plotting the running average vs the index of the data. The running average of the data for the fluctuating trap (σ = 10 nm) decays following $\beta_0/\sqrt{k}$ (the solid line). $\beta_0/\sqrt{k}$ is generated based on the theoretical value of ${\beta_0}^2$.

obtained from a control measurement of the power spectrum of the bead position (data not shown). The maximum allowed trap stiffness $k_{\max}$ was set at 9.8 fN/nm. The values of m_+ and m_- were then calculated using Eq. 2.29 for each value of σ^2. The bead was held 1 μm above a microscope cover glass resulting in a typical relaxation time of the bead in the trap of 10.16±0.04 ms (mean±s.e.m, N=3), at baseline stiffness. To generate a fluctuating input state trap positions were calculated using the recursive formula of Eq. 2.20 with ρ=0.95 and updated every 25 ms respectively. Simultaneous to resetting the trap position, the trap stiffness was adjusted so that Eq. 2.21 holds. Figure 2.1 shows the distribution of trap positions along with the trap stiffness corresponding to those positions. The bead positions were sampled every 50 ms, resulting in an effective autocorrelation of $\rho = 0.9025$, and were plotted as a histogram (Fig. 2.2). The signal variance S_0^2 is determined from the raw position data or its histogram by gaussian fitting.

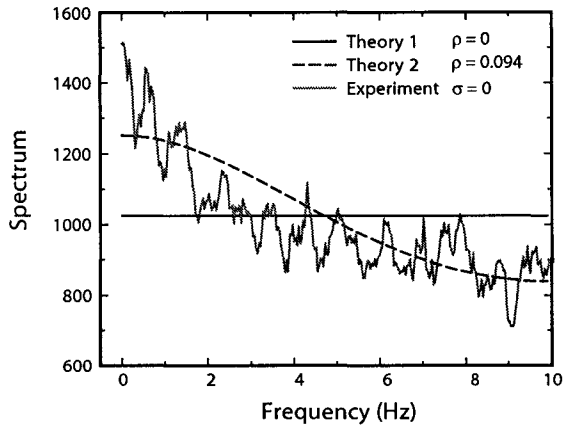

FIGURE 2.4. Power spectrum of the bead positions in case of no external noise ($\sigma = 0$). The experimental data modulates slightly in contrast to the initial prediction (theory 1 plot) where the power spectrum is expected to be flat. It agrees well with the theory 2 plot which is calculated with a correlation factor ρ as 0.094.

2.5 Analysis

As previously discussed, we consider two distinct measures of noise scale - the sample variance, S_0^2 and the variance of the estimation error, β_0^2. In general, the physical meaning of S_0^2 is clear and it can be easily acquired by either calculating the sample variance of the position data, measuring the width of a histogram, or integrating the one-side power spectrum. As illustrated in Fig. 2.2, the reduction in S_0^2 can be determined upon comparison of the histograms. The upper figure is the histogram of the bead position in case of stationary trap ($\sigma = 0$) and the bottom figure is the histogram in case of fluctuating trap ($\sigma = 10$ nm). A reduction in the sample variance is from 1087 ± 1 nm^2 to 764 ± 21 nm^2. On the other hand, ${\beta_0}^2$ may not be clear. In the time domain, we may understand the general property of ${\beta_0}^2$ by plotting the running average, M_k of the data in terms of the data index, k (since the data is discrete). The interpretation of ${\beta_0}^2$ is that if we plot the M_k vs. k, then we will see a general decay roughly like $M_k \sim \beta_0/\sqrt{k}$ (Fig. 2.3) and converged to the sample mean.

In the frequency domain, the sample variance, S_0^2 and the variance of the esti-

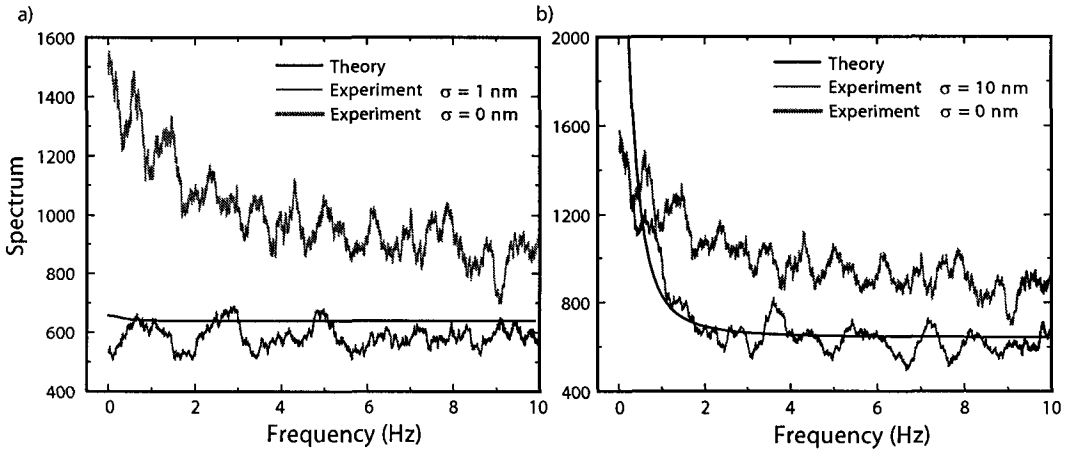

FIGURE 2.5. Power spectrum of the bead positions with external noise input (σ = 1 and 10 nm). a) The entire spectrum of σ = 1 is lying below that of σ = 0 which indicates that ${\beta_0}^2$ as well as S_0^2 decrease compared to ones at σ = 0. b) The spectrum of σ = 10 shows that increasing input noise actually results in increasing ${\beta_0}^2$. The spectrum of σ = 10 starts above at zero frequency and decays below the spectrum of σ = 0 for high frequency. It indicates that S_0^2 has been still reduced. Both experimental data (σ = 1 and 10) show good agreements with the theoretical predictions.

mation error, β_0^2 can be determined from the power spectrum analysis. The sample variance, S_0^2 can be obtained by calculating the total spectral power of the output signal (Eq. 2.18) and β_0^2 can be estimated from the power spectral density (Eq. 2.16 or 2.32) at zero frequency,

$$\beta_0^2 = 2\pi h(0). \tag{2.33}$$

We acquired the square amplitude of the fast fourier transform of the sample data which is an approximate form of the periodogram - the discrete estimate of $h(\omega)$. Afterwards, we smoothed the power spectrum using Daniell window which provides running average values with a given window size (N_w = 201). For the case σ = 0, the initial theoretical prediction is that the periodogram is flat over entire frequency range since there is no extra noise except for intrinsic noise (Fig. 2.4 (theory 1)). The measured power spectrum in Fig. 2.4, however, shows a slight modulation, which indicates that bead position data are slightly correlated. The correlation ρ is esti-

$\sigma^{2\ a}$	$S^{2\ b}_{exp}$	$S^{2\ c}_{th}$	$\beta_{0,exp}{}^{d}$	$\beta_{0,th}{}^{e}$
0.0	1087±1	1025	1512	1025
1.0	648±9	639	548	658
25.0	666±14	663	1110	1126
100.0	764±21	738	1577	2589

TABLE 2.1. Noise measures for correlated input noise, $\rho = 0.95$

[a]The variance of the trap position (nm^2)
[b]The measured sample variance (nm^2)
[c]The predicted sample variance (nm^2)
[d]The measured variance of the estimation errors (nm^2)
[e]The predicted variance of the estimation errors (nm^2)

mated as ≈ 0.094 using linear regression of the Y_k vs Y_{k+1} plot. We recomputed the spectrum based on this value and the sample variance (1087 nm^2). As shown in the Fig. 2.4 (theory 2), it agrees quite well to the experimental data.

For the case when the external noise is added with the correlation factor, 0.95, the reductions of S_0^2 for all conditions (σ = 1, 5, and 10 nm) are observed in the power spectra. When σ = 1 nm, the spectral density drops over the entire frequency range of interest (Fig. 2.5[a]). Thus, both S_0^2 and ${\beta_0}^2$ have been reduced. We also observed similar features for S_0^2 and ${\beta_0}^2$ when σ = 5 nm (data not shown). However, for larger fluctuations of the trap, *i.e.* when σ = 10 nm, the power spectrum peaked above baseline level at low frequencies but dropped below at higher frequencies. In other words, the integrated power or S_0^2 was reduced while ${\beta_0}^2$ had increased (Fig. 2.5[b]). When comparing our results, we find good agreement with theoretically calculated power spectra (Fig. 2.5). This illustrates that strictly seen noise suppression can be qualitatively interpreted in terms of the power spectrum analysis. On the other hand, the measurement of β_0^2 may be problematic since the power spectrum at zero frequency is prone to error (for σ = 10 nm the power falls below the theoretically predicted value) because of the limited amount of data. Besides, the power spec-

trum at zero frequency is very sensitive to the measurement offset errors. S_0^2, on the other hand is a more robust measure and less sensitive to these effects. Table 2.1 summarizes our results showing good agreement with theoretical predictions.

2.6 Conclusion

In this chapter, we have clarified the somewhat counter-intuitive phenomenon that noise may be used to reduce noise. Earlier discussion of this phenomenon have characterized the behavior as a nonlinear phenomenon, primarily due to the sufficient condition of Vilar and Rubí that the state dependence of the noise be locally concave down. However, such a characterization distracts from the essential ingredients required for noise suppression. The critical property for noise suppression is that added fluctuations have to drive the input into states with reduced intrinsic noise as shown in our experiment. Our example using an optically trapped bead clearly demonstrates this necessary condition and provides a simple intuitive understanding of how noise is reduced. This simple rule of thumb is particularly useful when considering the signal variance S_0^2 or cases where the input fluctuations are uncorrelated. ${\beta_0}^2$, however, does depend upon the correlation time of the input fluctuations and may have increased even though S_0^2 was reduced. In such cases, inspection of the full power spectrum of bead positions provides direct insight into such spectral properties of noise reduction. Finally, it is important to realize that we have not applied any negative feedback schemes in which the trap is positioned in response to bead displacement [30]. Here, the trap position was changed in a stochastic fashion independent of the bead position.

Chapter 3

Experiment of noise-induced escape from a sloshing potential well

Minimization of noise is always an issue in experimental measurements. In that context, we investigated the idea to reduce noise observed at the output of a physical system in the previous chapter (ironically, by adding noise at its input). However, there is one robust aspect of noise: it harnesses many biological, chemical, and physical reaction processes. Kramers first recognized this phenomenon as a noise-assisted hopping event across an energy barrier. Since then it has been of great importance to study how to characterize and control reaction rates in terms of noise. In this chapter, we demonstrate noise-activated escape processes experimentally using a simple physical system in which a microscopic bead is trapped in a double-well potential. We discuss how we can control the characteristics of the escape process by adding a periodic force and illustrate the characteristics in terms of the residence time distribution and the escape phase.

3.1 Introduction

Thermally activated escape processes are ubiquitous phenomena in nature and underlie fundamental processes in biology, chemistry, and physics. After Kramers seminal paper in 1940 [31], a wealth of (related) publications on the topic has emerged, including those in which thermal noise has been used to enhance the response to time-dependent external fields, a phenomenon named "stochastic resonance" [26, 32]. A recent and elegant example in biology is the folding and unfolding transitions of RNA hairpin loops under the influence of a mechanically applied force [33].

Optical traps are ideally suited for studying thermally driven escape processes [34,

35]: microscopic particles held in a trap in water undergo substantial thermal fluctuations depending upon the shape of the optically generated potential. For example, the potentials may be as shallow as just a few k_BT, enabling occasional escapes of the particles from the trap. A double-well potential exhibiting two minima separated by a barrier is readily generated by using two spatially separated optical traps. Well depth, barrier height and shape are determined by the laser power and the spatial separation of the traps, and a periodic external force can be applied by modulating the laser power appropriately. Thus far, most forced-escape experiments have mainly been performed in the limit of slowly varying fields, where the system is assumed to be in a meta-stable state. We go beyond this limit and use a broad range of driving frequencies to investigate the escape characteristics. In particular, we make measurements of particle position within the potential at high spatial and temporal resolution to determine the dependence of the escape phase on the driving frequency. This parameter has been of recent theoretical interest yet has not been investigated experimentally.

3.2 Experimental application

We use an intrinsically fluctuating and overdamped system in which a microscopic polystyrene bead (radius 0.245 $\pm$ 0.005 μm and mass $\sim 0.65 \times 10^{-16}$ kg) is confined in a double-well potential which is created by two optical traps [20]. Acousto-Optical deflectors (AODs, IntraAction Corp.) allow scanning of a laser spot from one position to the other at a rate ($\sim$100 kHz) well above those of interest in this experiment, i.e., the escape rate and the relaxation rate of the bead within the trap. Therefore, time-sharing effectively creates two spatially separated potential wells, of which we can both control position and depth, by controlling the frequency and amplitude of the AOD's acoustic driving signal, respectively. A second laser (wavelength 830 nm) is used to measure the position of the bead (resolution $\sim$1 nm) by recording the

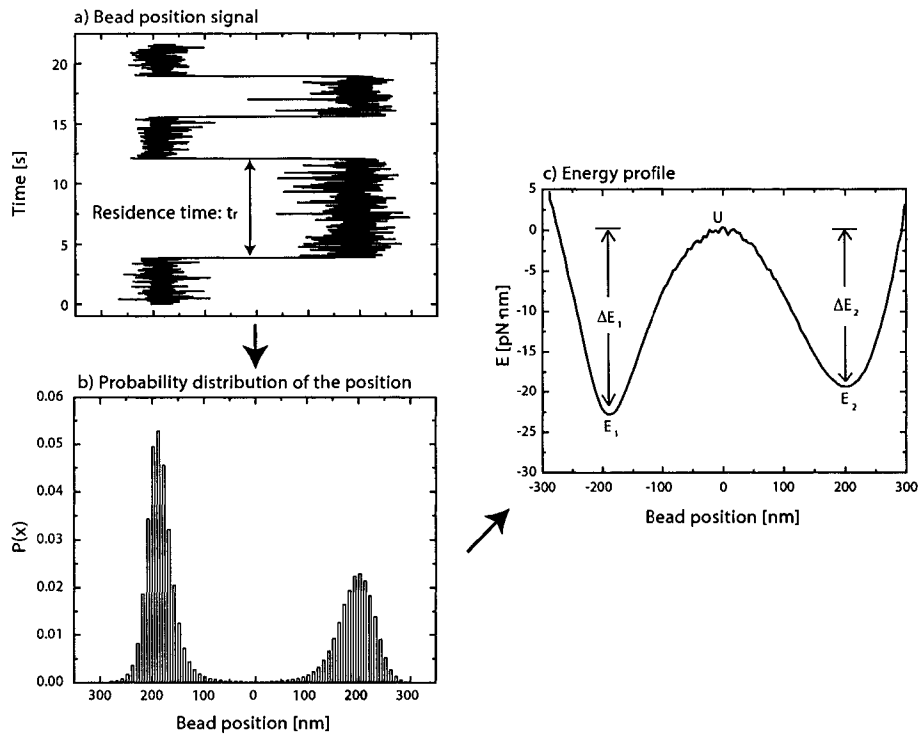

FIGURE 3.1. A double-well potential as calculated from the histogram of the bead position. a) The time snap of the bead position signal acquired from the position detector. b) The accumulated position signal are plotted into the probability distribution. c) The energy profile is calculated from the probability distribution. Wells are indicated by E_1 at $x_1 \sim -188$ nm and E_2 at $x_2 \sim 200$ nm, while the barrier top U is located at $x \sim 2$ nm. Barrier heights ΔE_1 and ΔE_2 are -22.9 ± 0.3 pN·nm and -19.7 ± 0.1 pN·nm, respectively. The barrier top appears noisier because the bead resides over the region less frequently. Data was sampled at 1 kHz.

deflection of forward scattered light with a quadrant photodiode [20]. The position sensor was placed at the center of the potential barrier so that its range covers both potential wells. This arrangement enables bead position measurements at spatial and temporal resolutions exceeding those obtained using conventional video imaging methods. As illustrated in Fig. 3.1, we first recorded bead positions in the absence of a driving field to characterize the potential (in one dimension for simplicity), which is readily calculated from the probability distribution of the bead position: $P(x) = \exp(-E(x)/k_BT)$. We can then extract the entire shape of the potential including the

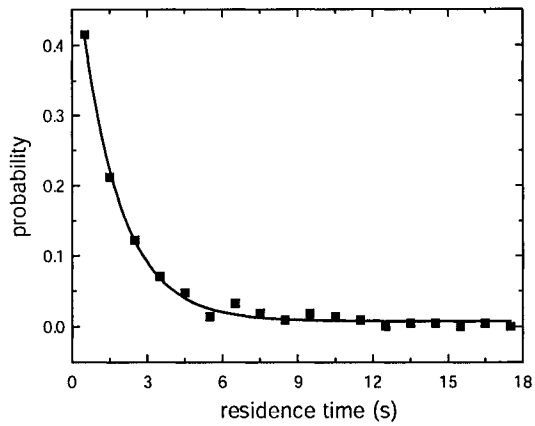

FIGURE 3.2. Residence time distribution in the E_2 without any external field present. The solid line (−) represents a fit of the data to a single-exponential decay function providing a mean residence time of $\widetilde{\tau}_k = 1.6 \pm 0.1$ s (N = 364 escapes)

height of the energy barriers, ΔE_1 and ΔE_2. The spring constants, k_{b1}, k_{b2} and k_u that characterize the shape of the potential wells and barrier, are determined by locally fitting a second order polynomial. These parameter values have been summarized in Table 3.1, and can be used to predict the Kramers time, τ_k for each of the wells using Kramers' formula,

$$\tau_k = \lambda^{-1} \sim \tau_r \exp(-\Delta E/k_B T). \tag{3.1}$$

τ_r is the system relaxation time,

$$\tau_r = \frac{(2\pi\alpha)}{\sqrt{k_b k_u}} \tag{3.2}$$

where α=$6\pi r\eta$ is the viscous drag coefficient, with r the radius of the bead and η the viscosity of water. The experiment was performed in water at room temperature (~296 K) with the bead center ~545 nm above the surface of the flow cell requiring a correction to the viscous drag to account for the presence of the wall.

Once the system has been fully characterized, we add the periodic external field with period τ_m in order to create the sloshing potential according to the following equation,

$$\alpha\dot{x} = -U'(x) + A\cos(2\pi t/\tau_m) + \sqrt{2\pi\alpha k_B T}\xi(t) \tag{3.3}$$

	ΔE(pN·nm)	k^a (fN/nm)	τ_r(ms)	τ_k(s)	$\widetilde{\tau_k}$(s)
E_1	-22.9±0.3	8.9±0.3	7.7±0.2	2.4±0.1	2.3±0.2
E_2	-19.7±0.1	4.4±0.1	11.0±0.2	1.5±0.1	1.6±0.1
U	-	-1.6±0.01	-	-	-

TABLE 3.1. parameters of the potential well shown in Fig 3.1. and characteristic time constants

[a]Spring constant

with x the system coordinate, $U(x)$ the potential, $\xi(t)$ a white noise, and $A\cos(2\pi t/\tau_m)$ the modulation. The amplitude of a modulation force can be considered either strong or weak depending on the effects on the escape process. Based on the theory by Maier and Stein [31, 36], there are two important physical lengths that play roles in the escape process: First, a diffusion length ($\sim \sqrt{2k_BT/U''(x_u)}$) which determines the layer which a particle must reach in order to escape over the potential barrier. Second, the oscillation length, which is determined by the applied force divided by the barrier curvature. When the applied force increases up to a critical force, this oscillation length becomes close to the diffusion length and the escape dynamics will be largely affected by the force modulation process. The critical force is determined by the equation [36],

$$F_c \approx \sqrt{2k_u k_B T}. \tag{3.4}$$

The critical force is ~ 0.11 pN in our system, whereas the modulation amplitude or force $A \simeq 6.7$ fN in all our experiments. It is weak forcing relative to the critical force. Hence the simple perturbative modification of Kramers' formula is likely to apply. Previously, the similar experiments were performed and succeeded to characterize the system dynamics in terms of the residence time distributions [34]. However, the dependence of the escape phase upon noise strength and modulation frequency has recently attracted attention and have been extensively discussed theoretically [37–40]. Here, we study the escape process by considering two different quantities: the

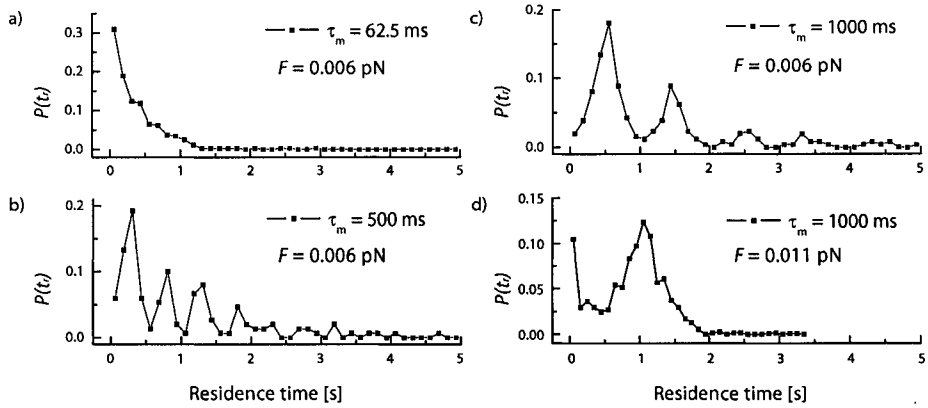

FIGURE 3.3. Residence-time probability distribution. a) at $\tau_r \leq \tau_m << \tau_k$, $P(t_r)$ looks like a simple exponential decay. b) and c) $\tau_r < \tau_m < \tau_k$, the odd harmonic structure is observed. d) at high modulating force F_m, the escape process is simply controlled by the external force. Most of particles will escape when the potential barrier is minimum regardless of the modulation period, τ_m.

residence time distribution and the escape phase. While the resonance time provides a general characteristics on the escape process upon the periodic force, the escape phase reveals the detailed dynamic relation between the periodic force, the escape process and the system.

3.3 Results

3.3.1 Residence-time distribution

The residence-time, t_r is readily obtained from time-series position signal data. It measures the time duration of the bead in a potential (Fig. 3.1). Without external force, we find that $P(t_r)$, the residence-time probability distribution exponentially decays (Fig. 3.2) following the Poisson distribution as

$$P(t_r) = \tilde{\tau}_k e^{-t/\tilde{\tau}_k}, \tag{3.5}$$

where $\tilde{\tau}_k$ indicates the mean residence time which is approximately τ_k in Eq. 3.1. We can then compare τ_k calculated from the profile of the potential to $\tilde{\tau}_k$ obtained by

fitting $P(t_r)$ with a first order exponential decay. For example, for the well E_2 we find that $\widetilde{\tau}_k = 1.6 \pm 0.1$ s which is in an excellent agreement with τ_k ($\sim$1.5 s). It indicates that our system is well within the Kramers limit, in other words, it is an overdamped meta-stable state.

Upon exerting periodic force, we find that $P(t_r)$ depends on the modulation period τ_m as well as the amplitude of the force. If the amplitude of force is very weak ($F_m = 0.006$ pN $\ll F_c = 0.11$ pN), we can distinguish the characteristics of the escape process in four different time regimes. First, if $\tau_r \leq \tau_m << \tau_k$, we observe a exponential decay (Fig. 3.3^a). In comparison to the probability without external force (Fig. 3.2), the maximum amplitude of $P(t_r)$ has decreased and $\tilde{\tau}_k$ also has become smaller (about 0.5 s). It is assumed that the system may not recognize the modulation of the potential in time due to the fact that τ_m is not bigger than τ_r and the escape process is affected by the intrinsic system dynamics. This effect can be further understood by investigating the escape phase (subsection 2.3.2). If $\tau_r < \tau_m < \tau_k$, we observe a structure of the odd harmonics. The physical interpretation is simple as modulation time is still short, the particle might not escape every τ_m but wait an extra period τ_m, $2\tau_m$, or nτ_m (Fig. 3.3^{b,c}). When $\tau_m \simeq \tau_k$, $P(t_r)$ shows a peak around $t_r \simeq \tau_m$ in the residence-time distribution (data not shown). This phenomenon is sometimes referred to as "stochastic resonance". In this regime, the majority of escapes occur before t_r reaches τ_k and is further assisted by the synchronized minimization of the potential barrier. For the case of $\tau_m \gg \tau_k$, the system will not wait until the potential barrier is at minimum and therefore, $P(t_r)$ will decay exponentially just like the case of no external force. If the amplitude of the force increases, the escape process becomes simply synchronized with the modulation force and show a peak at $t_r \simeq \tau_m$ regardless of τ_m. For example, $P(t_r)$ shows a peak at $\tau_m = 1000$ ms when $F_r = 0.011$ pN in Fig. 3.3^d in contrast to Fig. 3.3^c where $\tau_m = 1000$ ms but $F_r = 0.006$ pN.

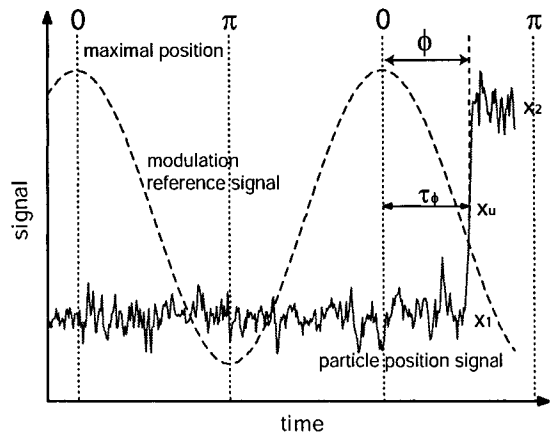

FIGURE 3.4. Determination of escape phase, τ_ϕ, expressed as a fraction of the modulation period τ_m. τ_ϕ equals the time from the point where the particle just passes the potential barrier top to the nearest previous maximum of the phase signal.

3.3.2 Escape phase

The escape phase is defined as indicated in Fig. 3.5. It is the time interval between the nearest previous maximum of the modulation reference signal and an escape event. The modulation reference signal can be readily obtained by low-pass filtering the AOD driving signal meanwhile making sure this filtering does not introduce its own phase shift. The modulation reference signal and bead position were simultaneously recorded enabling the determination of the escape phase. Furthermore, for determining the escape phase we have only considered the escapes from potential E_2 into E_1. Three time constants are of importance in the dynamical system: τ_r, the relaxation time of a bead in the potential well, τ_k, the Kramers time and τ_m, the modulation period of the external driving field. Previous studies have been performed under condition in which τ_m is chosen to be much smaller than τ_k but larger than τ_r [34, 35]. Here, we explore conditions in which τ_m may range from near to τ_k to τ_r. Results are presented in Fig. 3.5, where we show the escape probability versus the phase. In this case, a phase of $\tau_m/2$ corresponds to a minimum of the barrier height, and not surprisingly the escape probabilities peak around that point. However at

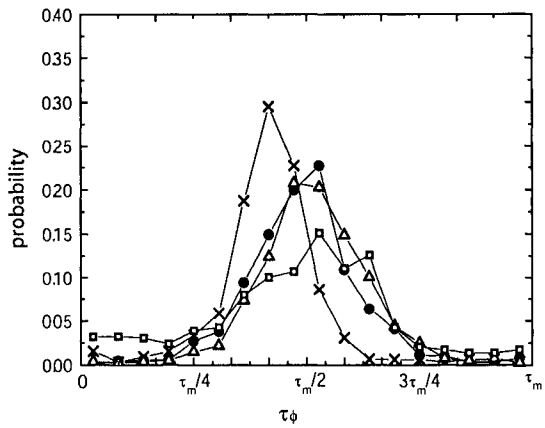

FIGURE 3.5. Escape phases. Shown are the probability distributions of escape vs. phase expressed in terms of τ_m. A phase of $\tau_m/2$ corresponds to a minimum barrier height for the transition from E_2 into E_1. τ_m = 1000 ms (×), 500 ms(•), 250 ms(△), and 62.5 ms(□).

modulation times close to the Kramers time (τ_m = 1 s and τ_k = 1.5 s), the maximum probability has shifted remarkably to the left. We think that when $\tau_m \ll \tau_k$, the escape probability due to the intrinsic noise (and not the modulation), remains constant during one modulation period. This means that during one modulation escape will mainly be controlled by the modulation and not the intrinsic noise. Therefore the escape will be largely in phase with the modulating resulting in a minimal phase shift. As τ_m becomes longer, the escape dynamics are more and more determined by the Kramers times, which means that escape may well occur before the barrier has reached a minimum. Obviously, in the limit of $\tau_m \to \infty$ one expects the same exponentially decaying probability distribution as shown in Fig. 3.2. Alternatively, when τ_m becomes considerably smaller than τ_k, but is still much larger than τ_r transitions preferably occur when the barrier is at a minimum. Thus, it is the driving force that determines the dynamics. When τ_m becomes even smaller and starts to approach τ_r the probability distribution starts to smear out, and starts to become asymmetric. This trend is in an agreement with Smelyanski *et al.* [38], who predict an asymmetric escape probability distribution when the system is incapable, i.e. too slow, to follow

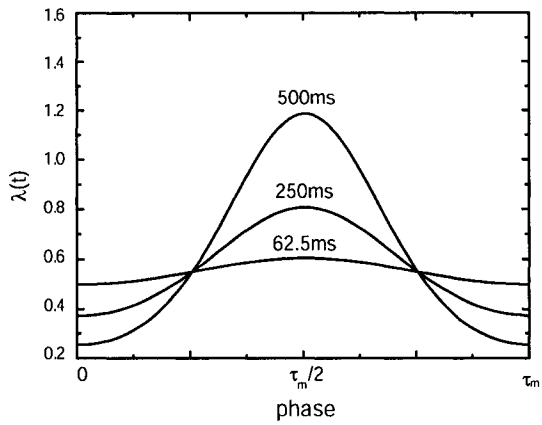

FIGURE 3.6. The modified Kramers escape rate λ(t) vs phase in terms of τ_m. It shows how the effective potential would change in different modulation times. The wash-out effect becomes clear when τ_m becomes close to τ_r.

the external field. The probability distribution broadens at high modulation frequencies because the system has insufficient time to explore the lowered barrier due to its finite relaxation time τ_r. In effect, what the system experiences is a modulated barrier that has been time-averaged over a period τ_r, in which case the transition probability distribution, or the instantaneous escape rate becomes:

$$\lambda(t) \cong \lambda_0 exp(- < \delta U(t)/k_B T >) \tag{3.6}$$

Here λ_0 is the Kramers rate in the non-modulated field, $1/\tau_k$. In Fig. 3.6, we calculated this rate based on the parameter values used in the experiment, and a similar, although not identical, broadening of the probability distribution is observed. However, this simple interpretation does not explain any emerging asymmetry. A more detailed study of this phenomenon at even higher modulation frequencies will be conducted but requires a different experimental set up, *i.e.* the time-sharing approach to generate the double-well potential is not practical at high modulation frequencies, for technical reasons.

3.4 Conclusion

We have studied the characteristics of the escape process using two approaches : phase relation between a driving external field and the escape of a Brownian particle over the modulated energy barrier and the residence-time probability distribution. In particular, we use novel experimental setup that enables tracking of the Brownian particle at high temporal bandwidth, fast modulation frequencies and accurate determination of the escape phase. At high modulation frequencies it was demonstrated that the Brownian particle does not experience the exact field modulation, but rather, due to its finite relaxation time, experiences an averaged modulation, resulting in a broadened escape probability distribution function. The observed phase shift and emerging asymmetry is consistent with theoretical predictions [38]. Further experimentation is required at shorter modulation times approaching the relaxation time, while investigating escape kinetics and phases as a function of noise strength remains an experimental challenge.

Chapter 4

THE ELASTIC PROPERTIES OF RANDOM COILED RNA AND THE EFFECTS OF IONIC CONDITIONS

The nucleic acids play key roles in their interactions with molecular motor enzymes such as DNA polymerases, RNA polymerases, and ribosomes. Thus, the study of their elastic properties has been an important part of the enzyme research as well as the main subject of the polymeric science. In our ribosome project, poly(U) is used as a template to understand the complicated mechanism of the ribosome translation. Since the property of this RNA molecule has not been well understood, it is preliminary to study the elastic properties of poly(U). We stretch individual poly(U) molecules and characterize them based on a worm-like-chain model. In addition, the effects of ionic conditions on the poly(U) molecule are studied with different concentrations of Na^+. Furthermore, other physiologically common ions such as Mg^{2+}, K^+, and spermine are also investigated. We find that at low salt concentrations the elasticity of poly(U) is not explained properly with a worm-like-chain model and the long range electrostatic interactions should be taken into account. We revisit the work done by Marko and Siggia who investigated the electrostatic interactions in double and single stranded DNA molecules [41, 42]. In the presence of spermine, a tetravalent polyamine, more complex behaviors are observed which should be further studied.

4.1 Introduction

The study of homopolymeric RNA is important in that it works as a model compound to derive and understand the properties of other more complex biopolymers. Since Grunberg-Manago and Ochoa discovered the enzyme called polynucleotide phos-

phorylase [43], synthetic homopolymeric RNA molecules have been studied extensively over decades [44–52]. And yet, these studies were methodologically based on the measurements of large ensembles of molecules. Consequently, the information was generally limited to the smooth averaged properties deficient of dynamic information. In general, thermal melting approach is less appropriate for understanding the mechanical properties of biopolymers and the reaction mechanism in which the mechanical properties of these molecules play important roles directing the reaction paths: for example, elastic properties of DNA and RNA, an mRNA unfolding process during the translation by ribosome, DNA unzipping by helicases, and unfolding RNA molecules with secondary structures. In that context, the single molecule study provides several advantages: it enables us to apply a force to a molecule locally and follow the trajectory of the molecule in time. In addition, an applied force can steer a reaction coordinate for the process in the direction along the force. Thus, the stretching of a biopolymer is an ideal way to investigate its elastic properties and further probe the interaction with enzymes. Double-stranded DNA (dsDNA) have been studied extensively using various single molecule techniques: optical tweezers, magnetic tweezers and AFM [3, 7, 53, 54]. Its elastic properties are well characterized by a worm-like-chain model [41, 55–57]. RNA, however, is structurally different from DNA in that it primarily exists as a single-strand in contrast to a double-stranded DNA helix. The absence of such stereochemical constraints allows RNA to have more degrees of freedom and to form extensive secondary and tertiary structural elements, such as hairpin loops and pseudo knots. For homopolymeric RNA molecules, although there is no complementary base-pairing, there are still base-pairing between same base components as well as base-stacking interactions which play primary roles in the formation of single and double helical structures of poly(A), poly(C) and poly(G) [44–46, 58]. Poly(U) also fold on itself and form a hairpin loop but only at low temperature [47]. At room temperature and at neutral pH, it is known to adopt a random coil conformation [48, 49], which makes poly(U) an ideal model system for studying the elastic

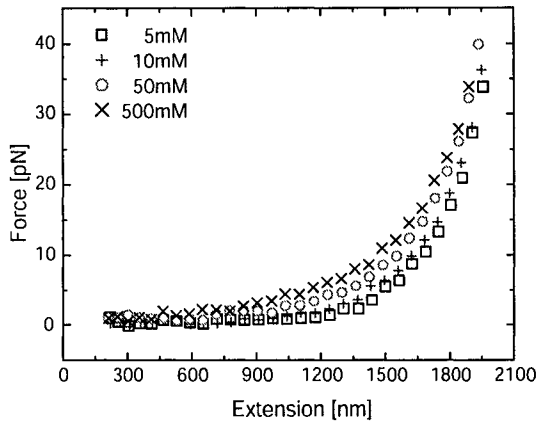

FIGURE 4.1. The ionic effect on the elasticity of poly(U): force vs. extension data sets in different [Na^+] show how it affects the elastic properties of the poly(U). The less force is required to stretch the same extension at lower [Na^+]. The step size of the piezo-driven stage is 5 nm, however, we only plot 50 points per curve to show clear distinctions between data sets for each ionic condition.

properties of polyelectrolyte with its highly charged phosphodiester backbone.

Electrostatic interactions between unshielded negatively charged phosphate groups generally stiffen the molecule causing the persistence length to increase [59, 60]. The total persistence length, as a result, can be decomposed into two contributions, an elastic persistence length due to the intrinsic elasticity and an electrostatic persistence length [41, 42, 61–63]. Screening of the charged phosphate groups will then particularly affect the electrostatic persistence. The electrostatic persistence length becomes important when the Debye screening length λ_D is of the order of or larger than the intrinsic elastic persistence length. The effective persistence length of dsDNA, which has an intrinsic elastic persistence length of ~50 nm, considerably larger than λ_D even at 5 mM Na^+ concentration, is approximately constant. This may explain why the force-extension data for dsDNA acquired at low salt concentration can be still well described with a simple worm-like-chain model that does not take into account the Debye-Hückel interactions [41]. On the other hand, in case of poly(U) the elastic persistence length is already of the order of λ_D at high salt concentrations. Hence, the electrostatic persistence length quickly becomes dominant and largely accounts

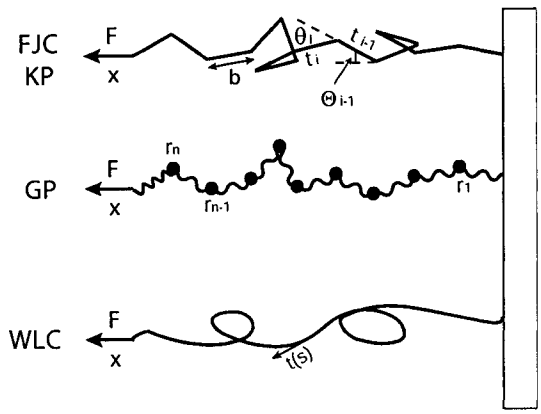

FIGURE 4.2. Schematic descriptions of polymer chain configurations. The upper polymer chain represents both the Kratky-Porod chain and the Freely-jointed-chain. The middle describes a Gaussian polymer. Consecutive segments are joined by a Hookean spring. The bottom one is for a worm like chain which is a continuous version of the Kratky-Porod chain. The arc tangent $\mathbf{t}(s)$ replaces the segments orientation vector, $\mathbf{t}$.

for the total persistence length when the concentrations of shielding ions are not sufficiently high. Thus, we observed that the force-extension relation for poly(U) depends highly on the [Na^+] (Fig. 4.1). In this chapter, we will discuss the theoretical models for biopolymers and investigate the elastic property of poly(U) at low salt as well as high salt concentrations.

4.2 Theoretical models

Poly(U) is a typical random coiled polymer in solution. Due to lacking of base-pairing and base-stacking interactions, it will adopt a random coil conformation to maximize entropy. There are several theoretical models to describe the elastic properties of a random coiled polymer. We will discuss the characteristics of some of them.

4.2.1 The Kratky-Porod model (KP)

This model was derived based on the polymer chain with no torsional stress [64]. If the polymer chain consists of N number of segments of length b and orientation vector $\mathbf{t}_i$, the energy of this chain configuration is

$$E_{KP} = -\frac{B}{b}\sum_{i=2}^{N}\mathbf{t}_i \cdot \mathbf{t}_{i-1} = -\frac{B}{b}\sum_{i=2}^{N}\cos\theta_i, \tag{4.1}$$

where θ_i is the angle between successive orientation vectors and B is the bending modulus. The characteristic length or the persistence length, L_p of the polymer is defined as a decay length of the angular correlation,

$$\langle \mathbf{t}_i \cdot \mathbf{t}_j \rangle = e^{-b|i-j|/L_p}, \tag{4.2}$$

with $L_p = B/k_BT$. It reflects the stiffness of the chain.

When stretching molecule, the external work is added to the energy,

$$E_{KP} = -\frac{B}{b}\sum_{i=2}^{N}\mathbf{t}_i \cdot \mathbf{t}_{i-1} - F\sum_{i=1}^{N}x_i = -\frac{B}{b}\sum_{i=2}^{N}\cos\theta_i - Fb\sum_{i=1}^{N}\cos\Theta_i, \tag{4.3}$$

where x_i indicates the extension of each segment along $\hat{x}$, the direction of force and Θ_i is the angle between $\mathbf{t}_i$ and $\hat{x}$ (Fig. 4.2). This model was solved only in the very low extension limit ($x \ll L$) [65] where x is the mean extension and L is the contour length of the chain defined by Nb. In this limit, x is described as $(2F/L_p)L/(3k_BT)$. This model is a basic compound for developments of other models.

4.2.2 The Gaussian Polymer model (GP)

Another elementary model is the Gaussian polymer model where each segment of the polymer is described as a particle connected by a Hookean spring. In particular, the distance between consecutive segments follow a Gaussian distribution with zero mean and a variance L_p^2,

$$\phi(\mathbf{r}_i - \mathbf{r}_{i-1}) = \left(\frac{3}{2\pi L_p}\right)^2 \exp\left(-\frac{3(\mathbf{r}_i - \mathbf{r}_{i-1})^2}{2L_p^2}\right), \tag{4.4}$$

where r_i indicates the position of a segment. The energy of this polymer upon exerting external force, F along $\mathbf{x}$ is

$$E_{GP} = \sum_{i=0}^{N} \frac{3k_BT}{2L_p^2}(\mathbf{r}_i - \mathbf{r}_{i-1})^2 - F\sum_{i=0}^{N}(x_i - x_{i-1}). \tag{4.5}$$

And the mean extension, x is expressed in terms of F,

$$x = \frac{NL_p^2}{3k_BT}F. \tag{4.6}$$

As a matter of fact, the Gaussian polymer is a spring with a chain stiffness $3k_BT/NL_p^2$. In general, this model is not particulary realistic for describing elastic properties of biopolymers since the model features a polymer which could be extended infinitely.

4.2.3 The Freely-Jointed-Chain model (FJC)

The freely-jointed-chain model shares similar features with the Kratky-Porod model except for the absence of a bending modulus, B. The chain consists of segments whose orientations are purely random without correlations. Hence the bending modulus which is defined as a correlation length times thermal energy, becomes zero. The energy of this model is simply the term only taking into account the change in x by the exerting force,

$$E_{KP} = -F\sum_{i=1}^{N} x_i = -Fb\sum_{i=1}^{N}\cos\Theta_i. \tag{4.7}$$

The mean extension upon force is then,

$$x = L\left[\coth\left(\frac{2FL_p}{k_BT}\right) - \frac{k_BT}{2FL_p}\right]. \tag{4.8}$$

It has been experimentally shown that this model is only applicable at low force and does not properly describe double stranded DNA. In order to correct the enthapic effect in the high force region, the model can be modified as

$$x = L\left[\coth\left(\frac{2FL_p}{k_BT}\right) - \frac{k_BT}{2FL_p}\right]\left[1 + \frac{F}{S}\right], \tag{4.9}$$

where S indicates a stretching modulus. Experimental data showed that the modified freely-jointed-chain model still failed to describe double stranded DNA, however, it worked relatively well for single stranded DNA [55]. Double stranded DNA is not a flexible molecule due to base pairing and stacking interactions and the typical correlation length is about 50 nm which corresponds to 147 bases which is why this model is not suitable. On the other hand, single stranded RNA or DNA have more degrees of freedom to move spatially and subsequently a short correlation length and a smaller bending modulus.

4.2.4 The Worm-Like-Chain model (WLC)

The worm-like-chain model is a continuous case of the Kratky-Porod model where the orientation vector, $\mathbf{t}$ is replaced by $\mathbf{t}(\mathbf{s})$, a tangential element along a curvature in terms of arc length, s. The energy is then expressed as,

$$E_{WLC} = \frac{L_p k_B T}{2} \int_0^L \left(\frac{d\mathbf{t}}{ds}\right)^2 ds - F \int_0^L \cos\Theta(s) ds. \tag{4.10}$$

It has been elegantly solved by Marko and Siggia in analogy with a quantum mechanical dipole problem [41] although it is not a simple analytical form for a direct application. The approximate formula was introduced by Marko and Siggia and later refined with additional correction terms by Bouchiat *et al* [41, 57]. The simple approximate form, so called the WLC, is written as

$$F = \frac{k_B T}{L_p} \left(\frac{1}{4(1 - x/L)^2} - \frac{1}{4} + \frac{x}{L} \right), \tag{4.11}$$

and for the latter formula, $\sum_{i=2}^{7} a_i x^i$ is added to the above equation with a_2=-0.5164228, a_3=-2.737418, a_4=16.07497, a_5=-38.87607, a_6=39.49944, a_7=-14.17718 which are derived by expressing the residuals of differences between the simple WLC formula from the numerical solution of exact worm like chain model. The worm like chain model has provided a precise description to a experimental stretching data of double stranded DNA compared to other models. However, the application of this

model has not been studied for the elasticity of a single stranded DNA or RNA which are assumed to be intrinsically different from a double stranded DNA.

4.2.5 The model for a polyelectrolyte

The conventional polymer models were derived based on polymers without any explicit electrostatic interactions between segments, in other words, the non-self-avoiding polymers. However, most of biopolymers are highly charged. In particular, DNA and RNA are composed of deoxyribose or ribose linked with negatively charged phosphoric acids. They affect the correlation length of the chain (the persistence length) with different characteristics dependent on the scale of intrinsic persistence length and the environmental ionic concentrations. In general, they stiffen a flexible polymer and increase the persistence length [59, 60]. We can define this kind of persistence length as an effective persistence length, A to distinguish from the persistence length, L_p of the non-self-avoiding polymer models. Analytically, A can be decomposed into the intrinsic chain stiffness (elastic persistence length), A_0 and the "electrostatic persistence" [61, 62] as

$$A = A_0 + \ell_{OSF}, \tag{4.12}$$

where ℓ_{OSF} is

$$\ell_{OSF} = \ell_B \frac{(\lambda_D \nu)^2}{4}. \tag{4.13}$$

Here ℓ_B is the Bjerrum length defined by $e^2/(\epsilon k_B T)$ with $\epsilon = 80$ in water, λ_D indicates Debye screening length which is roughly determined by $0.25/\sqrt{c}$ (c is a molar unit concentration of an environmental ion) and ν is the charge density of the ion. The idea of electrostatic persistence length was originally introduced by Odijk, Skolnick and Fixman [61, 62]. However we should note that the electrostatic interactions depend on the distance between electric charges, r and subsequently the extension of

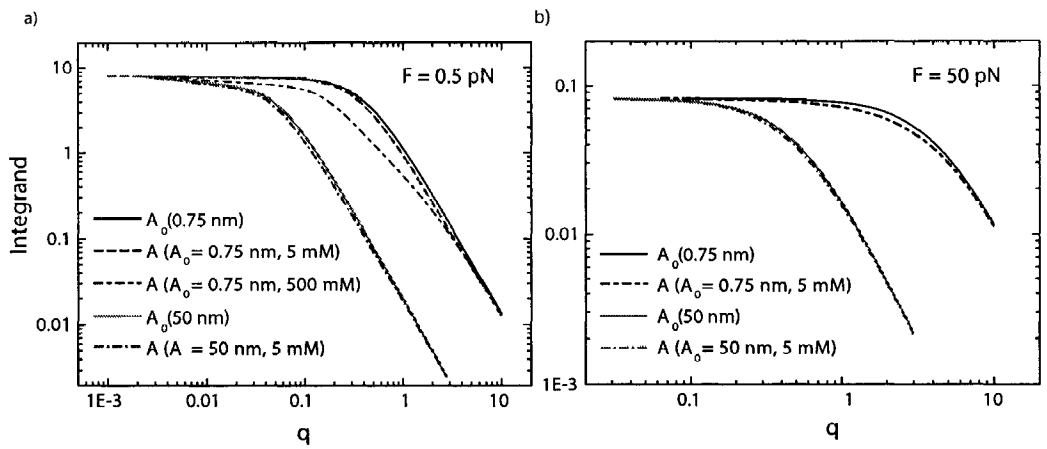

FIGURE 4.3. The characteristics of integrands in Eq. 4.17 at low force and at high force with a constant, A_0 and A. The integrands data are simulated with different conditions a) The integrand at $F = 0.5$ pN, the roll-off q of the integrand with A shifts to smaller q, compared to that of the integrand with A_0, which lead to the smaller area and consequently bigger extension is achieved at the same force. At 500 mM [Na^+], however, the shifted amount is very small indicating that less scale-dependency. Similarly, when the intrinsic persistence length is sufficiently larger than λ_D such as double stranded DNA whose typical persistence length is ~50 nm, the scale-dependency becomes negligible. The simulation plot for A with $A_0 = 50$ nm shows that the integrand is almost indistinguishable from the plot for $A_0 = 50$ nm. b) The difference between two integrands become smaller so does the scale dependency at high force (here at 50 pN).

polymers which is described by Debye-Hückel interactions,

$$V(r) = \frac{1}{r}\exp\left(\frac{-r}{\lambda_D}\right). \tag{4.14}$$

In other words, the contribution of electrostatic interactions to the effective persistence length will depend on the scale of extension between charged segments. Hence the electrostatic persistence length is rather scale-dependent than a constant as ℓ_{OSF}. In particular, the scale-dependency becomes stronger when the intrinsic persistence length of a polymer is an order of λ_D. As a matter of fact, it was necessary to revise ℓ_{OSF} for the case of flexible charged polymers [63]. The scale dependent persistence length is defined by,

$$A = A_0 + \ell_B \frac{(\lambda_D \nu)^2}{4} \mathcal{K}(q). \tag{4.15}$$

$\mathcal{K}(q)$ depicts the Debye-Hückel interactions for the different normal modes [41],

$$\mathcal{K}(q) = \frac{2}{\lambda_D^4 q^4}([1 + \lambda_D^2 q^2]\ln[1 + \lambda_D^2 q^2] - \lambda_D^2 q^2). \tag{4.16}$$

It was introduced into the WLC model [41] as,

$$\frac{x}{L} = 1 - \int \frac{dq}{2\pi} \frac{1}{Aq^2 + F/k_B T} + \frac{F}{S}, \tag{4.17}$$

with stretching modulus, S. The characteristics of the scale-dependency can be understood if we study the integrand of the formula. When the persistence length is simply A_0, the integrand $(1/A_0 q^2 + F/k_B T)$ behaves as a typical Lorenzian type power spectrum with a roll-off $q = \sqrt{(F/(A_0 k_B T)}$ at force, F. Now, when $\lambda_D \geq A_0$, the persistence length becomes scale-dependent and A replaces A_0 in the integrand. In the Fig. 4.3, we illustrate the characteristics of the integrands dependent on q, force, A_0, and ionic strength. The difference between two integrands decreases over force as illustrated in the simulation plots. When A_0 is large, or the ionic concentration is strong, the scale dependency decreases.

4.3 Experimentation

Data were obtained by stretching a single poly(U) molecule between a streptavidin-coated cover glass and anti-digoxigenin-coated polystyrene bead (dia. 0.49±0.024 μm) held with optical tweezers. Poly(U) molecules were polymerized from 5'-biotinylated oligonucleotides (U_{20}) using polynucleotide phosphorylase, and labeled at the 3'-end with digoxigenin using terminal transferase. A bead tethered to the cover glass was trapped and positioned 400 nm above the cover glass using a piezo-driven microscope stage (Physik Instrumente). A single poly(U) molecule was then stretched by laterally moving the piezo stage. Forces were determined by measuring the displacement of the bead from the center of the trap [20]. Force-vs-extension curves were calculated according to Wang *et al* [56]. Buffers (2 mM Hepes, pH 7.5) brought to the desired

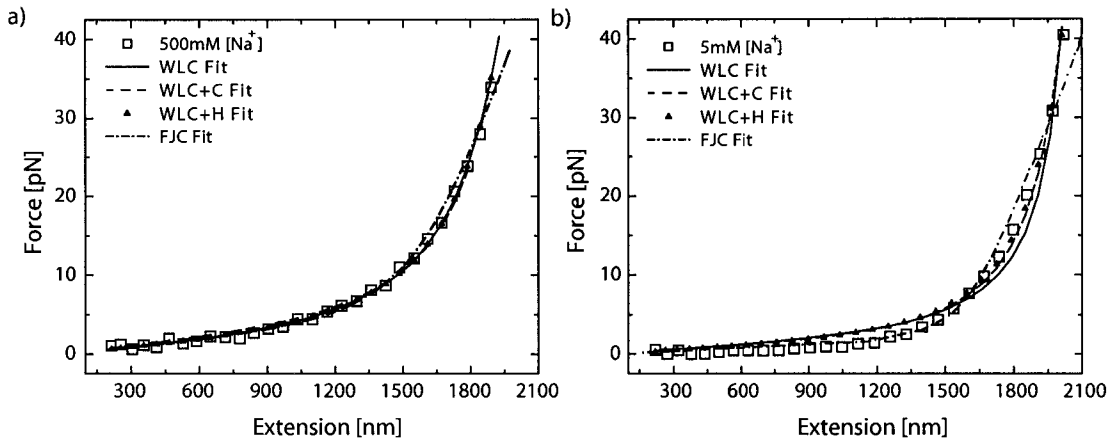

FIGURE 4.4. a) Data acquired at 500 mM [Na^+] is fitted with four different models. The results of fittings are summarized in Table 4.1. Except for slight deviations of WLC+C at the low force region and mFJC at the high force region, they all fit reasonably well. b) For 5 mM [Na^+], All models demonstrate significant deviations from the data.

Na^+ concentration using NaCl, were exchanged by washing the flow cell with ~10 times its volume. This enabled us to stretch the same individual molecule at different ionic conditions. Experimental procedures were validated by stretching dsDNA molecules of known lengths reproducing expected contour and persistence lengths (data not shown).

4.4 Result and Discussion

Prior to studying electrostatic effects, we investigated the intrinsic property of poly(U). We first analyzed the poly(U) stretching data acquired at 500 mM [Na^+] by fitting with 4 different models (we assumed that 500 mM would sufficiently minimize electrostatic repulsions between phosphate groups). The results are summarized in the Table 4.1. At high salt concentrations the force-vs-extension curves for single stranded DNA (ssDNA) were predicted by the modified freely jointed chain model

(mFJC) [55, 66],

$$x = L\left[\coth\left(\frac{2FL_p}{k_BT}\right) - \frac{k_BT}{2FL_p}\right]\left(1+\frac{F}{S}\right), \tag{4.18}$$

where L is a contour length, L_p is a persistence length, and S is the stretching modulus. Although poly(U) as ssRNA is expected to behave like ssDNA, upon fitting the mFJC (4.18) to the poly(U) data, we find a stretching modulus ($\sim$ 144 pN) much smaller than that of ssDNA (800 pN based on the mFJC fit and $\sim$ 2000 pN from WLC fit) [41, 55]. Considering the small difference between the backbones of ssDNA and RNA (deoxyribose lacks the 2'-hydroxyl group) such a large difference is not expected. Other three models used for fitting were developed from the following interpolation formula of the worm like chain model by different groups [41, 57],

$$F = \frac{k_BT}{L_p}\left[\frac{1}{4(1-x/L)^2} - \frac{1}{4} + \frac{x}{L} + \sum_{i=2}^{i\leq 7}\alpha_i\left(\frac{x}{L}\right)^i\right]. \tag{4.19}$$

Here α_i is the coefficients for the residuals as a seventh-polynomial [57]. We use abbreviations to distinguish each model. The WLC indicates the above interpolation formula (Eq. 4.19) without correction terms ($\alpha_i = 0$). The WLC+C refers to the above interpolation formula (Eq. 4.19). The WLC+H is the same as the WLC except for x/L being replaced by $x/L - F/S$ for the enthalpic correction. All three models fit to the 500 mM [Na^+] data quite well (Fig. 4.4[a]) and produce reasonable values of the persistence lengths and the stretching modulus (only for WLC+H). The contour lengths of WLC+H (2231±5 nm) and mFJC (1625±10 nm) are somewhat smaller than those of the WLC and the WLC+C. It makes sense that the part of extension comes from enthalpically stretching molecules over its contour length in these models. The models without stretching modulus can be regarded as for the case of $S \gg F$ and therefore the enthalpic contribution is very small to the extension of molecule in the most stretching experiments. All models fit to data reasonably well down to 200 mM [Na^+] but fail to fit below 100 mM [Na^+].

In the second part, we investigate the elasticity of poly(U) as polyelectrolyte. For

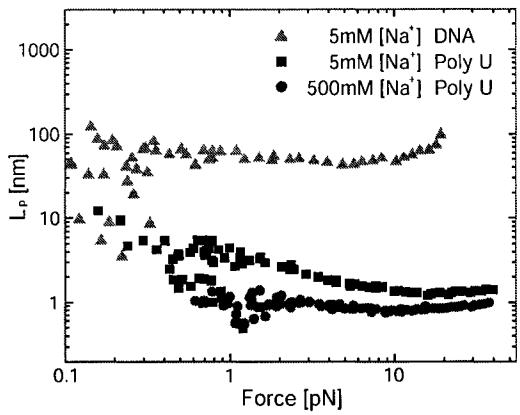

FIGURE 4.5. The L_p vs. force plot also shows that the elastic behavior of poly(U) deviates from the worm like chain model. The evidence of electrostatic effect on poly (U) elasticity is clear since L_p at 500 mM [Na^+] reaches to a constant persistence length more rapidly than at 5 mM [Na^+] and the L_p of DNA at 5 mM [Na^+] shows only small fluctuation over force as a typical worm like chain. (The contour length and persistence length of DNA are determined by the WLC+C fit (1), L = 1900±3 nm and L_p=55.0±4.6 nm).

a simple observation, it is clear that poly(U) becomes more easily stretchable with less [Na^+] (Fig. 4.1). In other words, the electrostatic repulsions make the persistence length get longer. However, the persistence length does not simply increase in terms of [Na^+]. When we plotted out the persistence length as a function of F (Fig. 4.5) obtained by rearranging Eq. 4.19 [55],

$$L_p = \frac{k_B T}{F}\left[\frac{1}{4(1-x/L)^2} - \frac{1}{4} + \frac{x}{L} + \sum_{i=2}^{i\leq 7} \alpha_i \left(\frac{x}{L}\right)^i\right], \tag{4.20}$$

we found that the persistence length of 5 mM [Na^+] decay slowly over the broad range of force to a constant in comparison to those of 500 mM [Na^+] and dsDNA. That explains why the data acquired at 5 mM [Na^+] cannot be fit very well with any of these model as shown in Fig. 4.4[b] since all these models were based on the elastic polymer with a constant persistence length. It has been known that if there are not enough shielding charges available, the long range electrostatic repulsions between charged segments strongly influence the elastic property of polyelectrolyte and the persistence become scale-dependent [41]. We follow Marko and Siggia in writing the

	WLC	WLC+C	WLC+H	mFJC
L(nm)	2327±3	2356±3	2231±5	1625±10
L_p(nm)	0.90±0.01	0.76±0.01	1.02±0.01	1.29±0.01
$< L_p >^a$(nm)	0.80±0.02	0.67±0.02	0.91±0.03	1.18±0.05
S(pN)	-	-	1512±8	145±7
$< S >^a$(pN)	-	-	1593±129	160±10

TABLE 4.1. Fitting parameters from different models: error indicates fitting error.

[a]Mean ± s.e.m. (N=10)

persistence length as having an elastic contribution and an electrostatic contribution,

$$A = A_0 + \ell_B \frac{(\lambda_D \nu)^2}{4} \mathcal{K}(q), \tag{4.21}$$

with A_0 the elastic persistence length, ℓ_B the Bjerrum length measuring the strength of the electrostatic interaction, λ_D the Debye screening length given by $1/\sqrt{8\pi c \ell_B}$ ($\sim 0.25/c^{1/2}$ nm) [41, 67], ν the effective charge density and c the concentration of Na^+ in molar unit. $\mathcal{K}(q)$ depicts the Debye-Hükel interactions for the different normal modes. Although no *ab initio* theory for ν exists, a phenomenological expression for ssDNA has been derived by Zhang et al. [67],

$$\nu = exp\,(\alpha + \beta\, c^{2/5}), \tag{4.22}$$

with $\alpha = 0.0338$ and $\beta = 1.36$ for ssDNA. The equation of the worm like chain model can be rewritten by replacing the constant persistence length L_p with a persistence length A that is scale and therefore force-dependent. For the relative extension it is then found [41],

$$\frac{x}{L} = 1 - \int \frac{dq}{2\pi} \frac{1}{Aq^2 + F/K_B T} + \frac{F}{S}. \tag{4.23}$$

The integrand can be approximated as $(Aq^2 + F/K_B T + \ell_B q^2/(1 + \lambda_D^4 q^2/4))^{-1}$ based on the weak dependence of extension on applied force [42].

For fitting, we use the analytical form of Eq. 4.23 which we derived using this

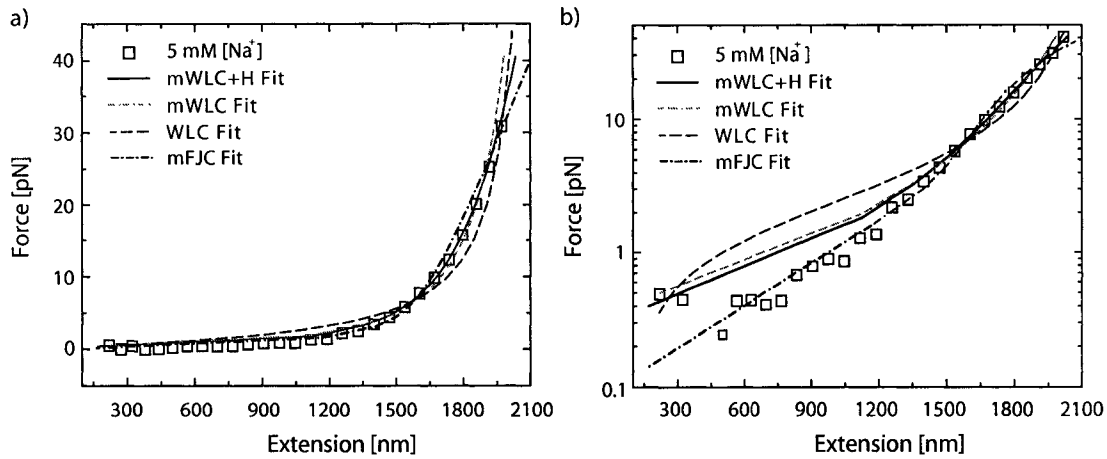

FIGURE 4.6. Fits to force vs. extension data acquired at 5 mM [Na^+]. The values of the fitting parameters found for each model have been summarized in Table 4.2. To better evaluate the fits to our data we show the a) linear and b) log-scaled plots.

approximate integrand and only use the data points for the relative extension, $x/L \geq 0.5$ due to difficulties in fitting at the low extensions ($x/L \leq 0.5$). In fact, this modified worm like chain model (mWLC) is known to be inaccurate for low extensions [41]. Mostly, we find that the mWLC can characterize the stretching data at 5 mM [Na^+] better than the other previous models (Fig. 4.6). We also fit without the enthalpic term (F/S) to investigate the significance of the stretching modulus in the mWLC. We notice the deviation at the high force regardless of [Na^+]. We obtain the elastic persistence lengths and the contour lengths from fitting with the mWLC and the mWLC without the last term (mWLC-S) and summarize in the Table 4.2. The acquired contour lengths from the fitting (2200±39 nm at 500 mM and 2160±54 nm at 5 mM [Na^+]) are smaller than what we obtain from the WLC and the WLC+C but close to that of the WLC+H. Consistently, the contour lengths of mWLC-S (2360±11 nm at 500 mM and 2336±13 nm at 5 mM [Na^+]) are very close to those of the WLC and the WLC+C. The elastic persistence lengths of all models are bigger at 5mM [Na^+] than at 500 mM [Na^+]. Interestingly, although the elastic persistence length A_0 for the mWLC is expected to be dependent on the intrinsic chain property rather

	500 mM		5 mM	
	mWLC	mWLC-S	mWLC	mWLC-S
L(nm)	2220±39	2360±11	2160±54	2336±13
A_0(nm)	0.75±0.03	0.67±0.01	1.24±0.16	0.92±0.03
$< A_0 >^a$(nm)	0.68±0.02	0.60±0.01	1.48±0.11	0.88±0.03
S(pN)	710±202	-	549±148	-
$< S >^a$(pN)	645±74	-	524±74	-

TABLE 4.2. Fitting parameters from modified worm like chain models

[a]Mean ± s.e.m. (N=10, 500 mM ; N=15, 5 mM)

than the electrostatic effects, it increases at lower [Na^+]. At this point, we do not know whether A_0 is locally affected by the electrostatic repulsions or it is simply chosen from the result of fitting procedure to minimize the reduced χ^2.

Interestingly, at relatively low concentrations of divalent counterions (2.5 mM [Mg^{2+}]), poly(U)'s force-extension data are predicted by the simple WLC model (data not shown), whereas this model is a poor description at ~80x times higher concentrations of Na^+. This strong effect of Mg^{2+} is not immediately clear from the presented expressions, but is mainly due to the dependence of $\mathcal{K}(q)$ upon λ_D. Simulations using the mWLC model proved consistent with our observation and predict non-scale-dependent persistence lengths at low [Mg^{2+}].

In the presence of spermine, a tetravalent polyamine (10 mM [Na^+], 0-10 μM spermine concentration), we have observed a variety of rather more complex behaviors. The persistence length sometimes is reduced presumably due to screening of poly(U)'s backbone charges. However, other molecules within the same preparation may display an increased persistence length, which may be an indication of charge inversion by spermine [68]. Figure 4.7 shows an example of a force-extension measurement in the presence of spermine (10 mM [Na^+], 10 μM spermine concentration). The data indicate the unfolding of a secondary structural element, presumably a hair-

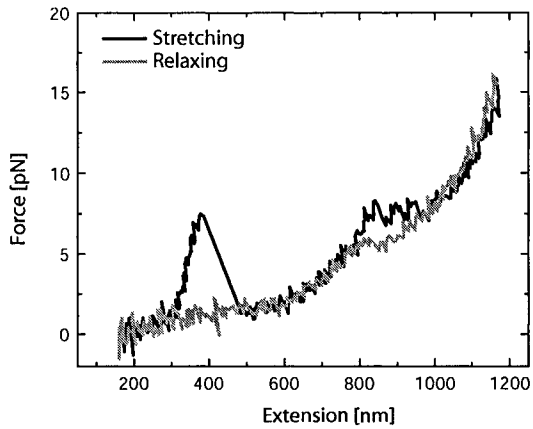

FIGURE 4.7. Force-extension data of poly(U) at 10 mM Na^+ and 10 μM spermine concentrations. The piezo stage was moved at a rate of 200 nm s^{-1} resulting in considerable hysteresis, indicating relatively slow folding kinetics of the poly(U)- spermine complex.

pin loop, at low force. This observation is consistent with X-ray fiber diffraction data of poly(U)-spermine complexes displaying structures similar to the A-form of dsDNA, thus indicating that the poly(U)-spermine complex adopts a double-helix conformation with both strands oriented anti-parallel [69]. At high force a second more gradual transition occurred. However, it is not clear what structural rearrangement this represents. It does not have the typical signature of an unfolding hairpin, neither does it display a typical helix-random coil transition like we have observed in poly(A) (unpublished data). The complexity of the observed unfolding behaviors within a very narrow range of polyamine concentrations warrants a more detailed future investigation of this phenomenon.

4.5 Conclusion

Poly(U) is a very flexible molecule with the persistence length smaller than 1nm and it behaves more close to a worm like chain rather than a freely joint chain. Presumably, there are still unaccounted restrictions present to limit the movements of bases. Owing to its small persistence length, poly(U) is largely affected by the

long range interactions between negatively charged phosphate moieties which should be accounted for the proper description of its elastic property. The mWLC which takes into account the interactions by incorporating the scale-dependent persistence shows a good tendency to characterize the elasticity of poly(U). However, it still shows slight deviations from the data especially for low extensions, which will be further to be studied. In future, it will be interesting to study the elastic properties of heterogeneous ssRNA as well as other homo-polymeric ssRNA rather than poly(U).

Chapter 5

THE STRUCTURAL ANALYSIS OF RNA HELICES

The foregoing chapter has focused on the elastic properties of the random coiled polymer, poly(U). In this chapter, we study two other homopolymeric molecules - poly(A) and poly(C). We stretch individual molecules and investigate their structural properties. Using a two-state model, we found that poly(A) and poly(C) form single-stranded helices with about 9 bases per turn and 8 bases per turn, respectively, at neutral pH and 500 mM [Na^+]. Upon stretching, the helices are unfolded into random coils and the free energy differences between two conformational states are 20 pN·nm for poly(A) and 17.5 pN·nm for poly(C).

5.1 Introduction

Four main types of homopolymeric RNA exist: polyadenylic acid (poly(A)), polycytidylic acid (poly(C)), polyguanylic acid (poly(G)) and polyuridylic acid (poly(U)). Due to the lack of complementary base-pair interactions, structures of these molecules display more variety than double stranded DNA or RNA and have been examined with various methods: circular dichroism, hypochromism, x-ray diffraction and nuclear magnetic resonance spectroscopy [44–52]. These studies have uncovered many interesting structural features: first, the sugar phosphate backbone of RNA is conformationally different from that of DNA due to the presence of hydroxyl group in $C_{2'}$ ribose, which imposes more rotational restrictions along the backbone. Second, different homopolymeric RNA molecules have significantly different conformations, which indicates that bases contributes to the formation of structure. For example, poly(U) exists mostly as a random coil at room temperature but develops secondary

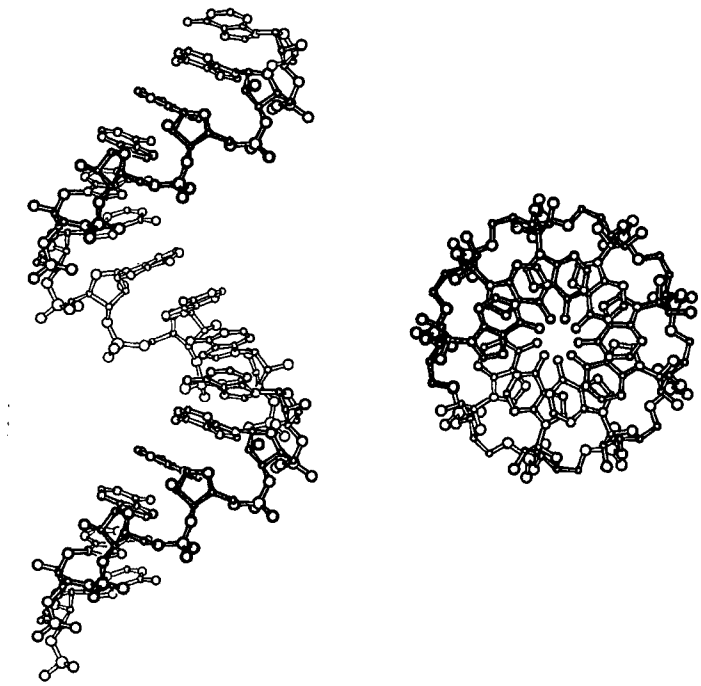

FIGURE 5.1. Proposed structure of poly(A) single-stranded helix on the basis of a single crystal study of the trinucleotide diphosphate (ApApA) [58]. Bases are in *anti* orientation (turned inside) and stacked parallel to each other. This helix contains 9 nucleotides per one pitch of 2.54 nm. Reprinted with permission from Wolfram Saenger

structures at low temperature [47]. On the other hand, poly(A) and poly(C) are able to form single- or double-stranded helices at room temperature dependent on pH condition. Poly(G) can exist as a quadruple helix and is able to form gels from aqueous solutions, which makes it difficult to synthesize and study individual molecules of poly(G). Thus, we do not include poly(G) in this study and discuss two readily available RNA molecules: poly(A) and poly(C).

Possible conformations of poly(A) and poly(C) were suggested as following: at pH ≤ 4.0, poly(A) is protonated at adenine N_1 and aggregates to form a double helix [70]. The poly(A) double stranded helix shows different features from Watson-Crick double stranded RNA or DNA: a dyad axis coincides with the helical axis and arrange the poly(A) chains parallel to each other, whereas the strands in DNA are oriented

anti-parallel. The helix is eight-fold and the pitch height is 3.04 nm. On the other hands, at neutral pH, poly(A) forms a single-stranded right-handed helix, with a helical pitch containing 9 bases which spans 2.54 nm (Fig. 5.1) [58]. Single-stranded poly(A) molecules are also found in nature usually linked covalently to the 3'-end of nuclear RNA, eukaryotic messenger RNA, and many viruses. These poly(A) tails serve a special purpose to protect these RNA molecules from being degraded and enhance translation [2].

For poly(C), two different single-stranded conformations were suggested. First, according to a NMR study, it might form a left-handed single helix with eight nucleotides per turn of 2.32 nm in neutral aqueous solution [71]. Secondly, an X-ray fiber diffraction study of poly (2'-O-methyl-C) which has similar thermodynamic and spectroscopic properties as poly(C) [72, 73] suggested that poly(C) might form a right-handed single helix with 6 nucleotides per turn [74]. At acidic pH ($\leq$4.5), poly(C) forms a double-stranded helix with parallel chains [45] similar to the parallel chain conformation of the poly(A) double-stranded helix. These secondary structures of poly(A) and poly(C) are transformed into random coils when temperature is increased above their melting temperatures, which indicates that these molecules can exist in two different structural states. Such experiment revealed the free energy changes and equilibrium constant of the conformational transitions [44, 45]. Nonetheless, these kinds of ensemble-average approaches usually lack details about the dynamics of the transition mechanism because it is difficult to synchronize large amount of molecules. Moreover, the mechanical properties of the molecules which play important roles in determining the molecules' conformations and subsequently conformational transitions cannot be fully understood using these approaches. In that context, the single molecule techniques where force will be exerted locally to the molecule have advantages. In particular, the application of a force to the molecule imposes a well-defined trajectory in the time course of the reaction process. In addition, it enables us to affect the rate of the reaction.

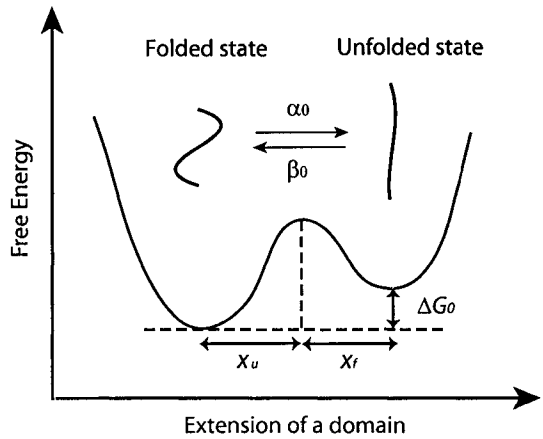

FIGURE 5.2. Illustration of the two-state model: The single-stranded helical structures of poly(A) and poly(C) can be described by the two-state model in that one helical pitch is considered as a domain with two possible states: folded or unfolded. ΔG_0 indicates the free energy difference between the unfolded and folded states. α_0 and β_0 are the rate constants for unfolding and folding at equilibrium. x_u and x_f are the activation barrier widths for the unfolded and folded states

A "simple" way to apply a force is by stretching a molecule. Upon stretching, a molecule (poly(A) or poly(C)) is extended and eventually unwound into a random coil. Thus, the force-vs-extension behavior reveals the elastic properties and the embedded kinetics as well as the thermodynamics of the conformational transition. The two conformational states (folded, unfolded) can be described as two stable minima of a double-well potential. Such a simple model would hold, were it not for the entropic elasticity of the molecule. To account for the free energy change upon extension of the molecule, a WLC model for polymer elasticity has been included. In case of poly(A) or poly(C), we can consider the chain as a system containing an ensemble of domains which have two possible states: the folded state (helix) or the unfolded state (random coil) as illustrated in Fig. 5.2. When exerting a force, we extend the molecule and eventually induce the conformational transitions of individual domains. Therefore the force-vs-extension data contains not only the elastic and structural properties but also the force-dependent unfolding and folding probabilities of domains. Based on this information, we can calculate the equilibrium constants, unfolding rates, and

the reaction coordinate profiles.

5.2 Materials and methods

5.2.1 Preparation of RNA and Sample.

Both RNA molecules ((poly A) and (poly C)) were prepared by elongating primers (20-mer, 5'-end biotin-labeled oligo uridylic acid (Dharmacon)) using polynucleotide phosphorylase (Sigma) to a length of $\sim$ 5 kb. The 3'-end of RNA was labeled with digoxigenin using terminal transferase (Invitrogen). 0.25 nM of differentially labeled RNA were incubated for 3 hrs with 12.5 pM of anti-digoxigenin (Roche) coated aldehyde-sulfate polystyrene beads (diam. 0.49$\pm$0.025 μm; Interfacial dynamics) in incubation buffer (2 mM Hepes, pH 7.0, 500 mM NaCl, with 0.3% w/v acetylated BSA) at 4°C (total volume is 100 μl). A microscope sample cell was made with a streptavidin coated coverslip (Xenopore) secured on to a microscope slide (VWR) using epoxy. 30 min after introducing the bead and RNA mixture into a sample cell allowing the 5'-ends of the RNA molecules to bind to the surface so that tethers are formed, excess unbound beads were removed by flushing with 500 μl of incubation buffer.

5.2.2 Measurement of force and extension

Tethered beads were trapped using optical tweezers and positioned such that the center of the bead was $\sim$400 nm above the anchor point. The initial height of a trapped bead was determined based on the relationship between the height of the bead and the intensity of the scattered light on to the photodiode [75]. The lateral position of a trapped bead relative to the trap center was measured by analyzing the detection of forward scattering light on a photodiode [20]. The stiffness of the optical trap was determined using the equipartition theorem by acquiring the mean

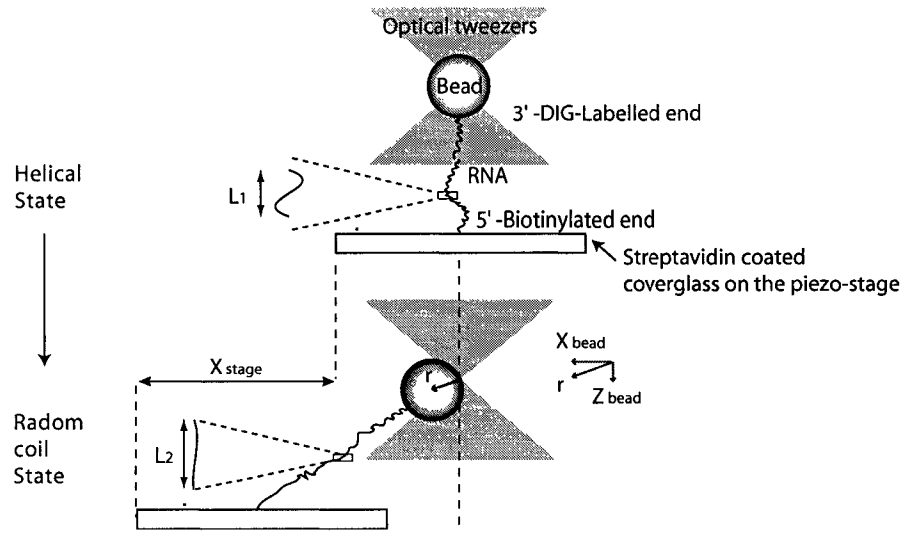

FIGURE 5.3. Schematic diagram of experimental system. The setup, consisting of the RNA molecule anchored to the streptavidin coated microscope coverslip and tethered to the anti-digoxigenin coated bead. The bead is trapped in the optical tweezers. The RNA molecule is pulled by moving the anchor point away using the piezo-driven stage. The movement of the bead from the center, $\mathbf{X_{bead}}$ is measured. $\mathbf{Z_{bead}}$ and the total extension, x are calculated in terms of $\mathbf{X_{bead}}$ and $\mathbf{X_{stage}}$(refer to Material and methods section). When the RNA molecule is stretched, the domains composed of the chain undergo conformational transitions from the helix with the contour length, L_1 to the random coil with the contour length, L_2.

square displacement of a trapped bead (not tethered) [20]. Force was exerted on the RNA molecule by moving the piezoelectric stage away from its initial position (Fig. 5.3). The force and the molecule's extension were calculated following the procedure developed by Wang *et al* [56]. The piezo-driven stage is set to move at 0.2 μm/sec.

5.2.3 Fitting with a two-state model

Many biological processes can be described by a simple two-state model, for example, protein and RNA hairpin unfolding, double-stranded DNA unzipping, and ligand binding to macromolecule [33, 76, 77]. In this model, the system can be described as a double-well potential with two stable minima as illustrated in Fig. 5.2. We can

characterize the system by modulating the potential barrier by changing variables such as temperature, pressure, and force. In single-molecule stretching experiment, we use force as a variable. Upon exerting force, the free energy difference between two states, ΔG changes as,

$$\Delta G = \Delta G_0 - F\Delta x, \tag{5.1}$$

where ΔG_0 is the free energy difference between two states at zero force and Δx is the extension change of the molecule. In case of a single-stranded helix, we regard one helical pitch as a domain with two possible states, a folded state (helix) with a contour length, L_1 and an unfolded state (random coil) with a contour length, L_2. The total contour length of the molecule is then given by $L = L_1N_1 + L_2N_2$ where N_1 and N_2 indicate the number of helical and random coil domains, respectively. Upon applying a force, F, the total extension becomes $x(F) = x_1N_1 + x_2N_2$. Here, x_1 and x_2 are extensions of the helical and random coil domains, respectively which are calculated from a worm-like-chain model without enthalpic correction terms:

$$x_i = L_i\left(1 - 0.5\sqrt{\frac{k_BT}{L_{p,i}F}}\right), \qquad i = 1, 2. \tag{5.2}$$

If we assume that the folding/unfolding process of individual domains represents a two-state process, N_1 and N_2 are related by

$$\frac{N_2}{N_1} = \exp\frac{-\Delta G(F)}{k_BT}, \tag{5.3}$$

where $\Delta G(F) = \Delta G_0 - F(x_2 - x_1)$ [77]. If the total number of domains, N is the sum of N_1 and N_2, the total extension, $x(F)$ can be rewritten as

$$x(F) = \frac{N}{1 + exp(\frac{-\Delta G(F)}{k_BT})}(x_1 + exp(\frac{-\Delta G(F)}{k_BT})x_2). \tag{5.4}$$

Using this equation, we can fit the force-vs-extension data and determine $L_{p,1}$ (the persistence length of a helical domain), $L_{p,2}$ (the persistence length of a random coil domain), L_1, L_2, ΔG_0 (free energy required to transit the states without external force), as well as N.

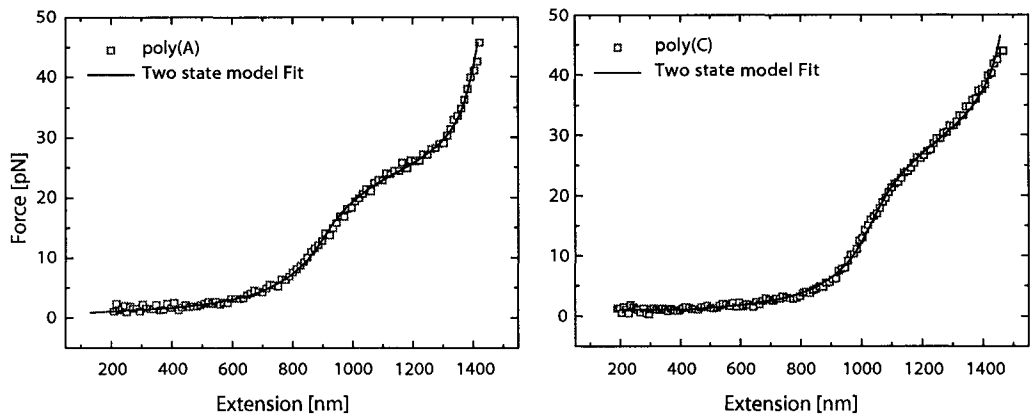

FIGURE 5.4. Force vs. extension plots of poly(A) and poly(C) and fits to the two-state model. a) Parameters of poly(A) from fitting are $L_{p,1}$ = 1.4 nm, $L_{p,2}$ = 0.7±0.1 nm, L_1 = 3.6±1.2 nm, L_2 = 5.3±1.4 nm, ΔG_0 = 24.8±13.0 pN·nm, N = 323±106 helices. The expected contour length is 1718±731 nm. b) Parameters of poly(C) from fitting are $L_{p,1}$ = 2.1±0.1 nm, $L_{p,2}$ = 0.6±0.4 nm, L_1 = 3.2±1.0 nm, L_2 = 4.7±1.1 nm, ΔG_0 = 19.5±10.8 pN·nm, N = 385±113 helices. The expected contour length is 1810±684 nm.

5.3 Results and Discussion

5.3.1 Structural properties and transition thermodynamics

Structural properties A total of 35 poly(A) and 18 poly(C) molecules was stretched. The force-extension data for one poly(A) and poly(C) molecule are shown in Fig. 5.4. These data show distinctive kinks indicating a structural transition (Fig. 5.4). Individual stretching data were fitted with the two-state model and the averages values of the fitting parameters for poly(A) and poly(C) are summarized in Table 5.1. In order to investigate the validity of the proposed helical structures, two different settings for the contour length, L_2 were used in the fitting procedure: one as a free fitting parameter and the other as a fixed fitting parameter (5.04 nm for poly(A) and 4.48 nm for poly(C)) based on the proposed models and the known contour length per base, 0.56 nm (which should be distinguished from the inter-phosphate distance (0.59 nm) [78]). From the first fitting procedure where L_2 is set as a free parameter, we

	poly(A)	poly(A)[a]	poly(C)	poly(C)[b]
$L_{p,1}$ (nm)	1.52±0.06	1.58±0.09	2.54±0.12	2.51±0.12
$L_{p,2}$ (nm)	0.75±0.04	0.71±0.04	0.66±0.05	0.74±0.09
L_1 (nm)	3.38±0.07	3.41±0.04	2.96±0.10	3.06±0.05
L_2 (nm)	4.93±0.08	5.04	4.35±0.11	4.48
ΔG_0 (pN·nm)	20.2±0.3	20.0±0.4	17.5±0.8	18.3±0.8

TABLE 5.1. The two-state model fitting parameters : They represent the structural properties of each state. Mean±s.e.m. (N=35, Poly(A); N=18, Poly(C))

[a] L_2 fixed as 5.04
[b] L_2 fixed as 4.48

find that L_1 are 3.38 nm for poly(A) and 2.96 nm for poly(C). L_2 becomes 4.93 nm for poly(A) and 4.35 nm for poly(C). These contour lengths correspond to 8.8 bases per domain for poly(A) and 7.8 bases per domain for poly(C). $L_{p,1}$ for poly(A) is 1.52 nm which is almost twice bigger than $L_{p,2}$ = 0.75 nm. Similarly, $L_{p,1}$ (2.54 nm) for poly(C) is larger than $L_{p,2}$ (0.66 nm). No appreciable difference in fitting result was found when L_2 was either a fixed or free parameter. In comparison to the previously proposed models, the acquired L_1s are quite larger than the predicted values (2.54 nm for poly(A) and 2.32 nm for poly(C)) while bases per domain calculated from L_2s are consistent to the predicted values.

Two-state probability We calculated N_2/N, the fraction of unfolded domains which represents the force-dependent unfolding probability using Eq. 5.3 and the two-state fitting parameters (Table 5.1). As shown in Fig. 5.5, we fit N_2/N with the following equation,

$$\frac{N_2}{N} = \frac{1}{1 + e^{E/k_B T}}, \tag{5.5}$$

with $E = \Delta G(F_{1/2}) - F\Delta x(F_{1/2})$ where $F_{1/2}$ is the force at which $N_2/N = 0.5$. $\Delta G(F_{1/2})$ and $\Delta x(F_{1/2})$ are the free energy required and the extension when a half of the domains are unfolded. For poly(A), we found $\Delta G(F_{1/2})$ = 27.1±0.4 pN·nm and

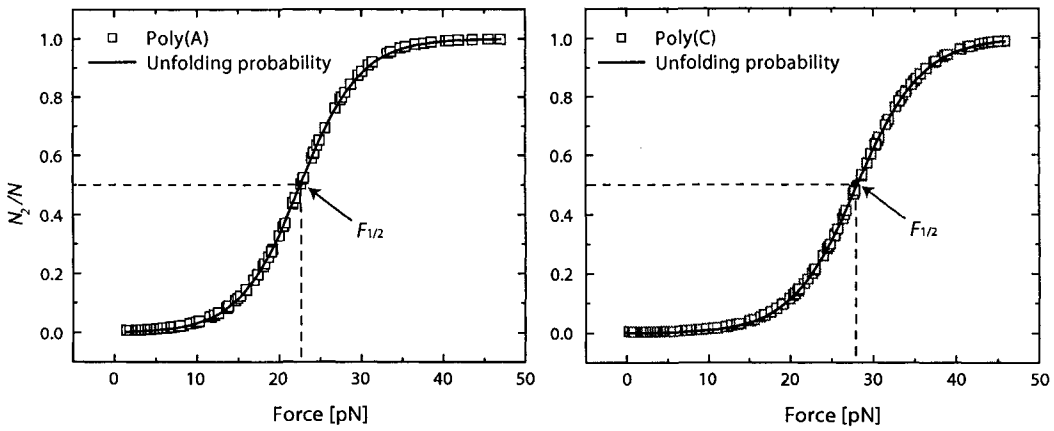

FIGURE 5.5. The fraction of the unfolded domains vs Force. We can obtain $\Delta G(F_{1/2})$ and $\Delta x(F_{1/2})$ by fitting N_2/N with Eq. 5.5 which characterize the unfolding probability. In these plots, $G(F_{1/2})$ = 24.6±0.1 pN·nm and $x(F_{1/2})$ = 1.1 nm for poly(A). $G(F_{1/2})$ = 28.7±0.1 pN·nm and $x(F_{1/2})$ = 1.0 nm for poly(C). $F_{1/2}$ is the force at $N_2/N = 0.5$

$\Delta x(F_{1/2})$ = 1.22±0.02 nm. For Poly(C), $\Delta G(F_{1/2})$ = 26.5±0.7 pN·nm and $\Delta x(F_{1/2})$ = 1.02±0.02 nm. Consequently, $F_{1/2}$ calculated for poly(A) is 22.2±0.5 pN and for poly(C) is 26.0±0.9 pN. It should be noted that $\Delta G(F_{1/2})$ is contributed to by not only ΔG_0 but also by the entropy change between the folded and unfolded states at $F_{1/2}$. When we subtracted the entropic contribution from $\Delta G(F_{1/2})$ which is the energy difference between a helix and random coil, we found ΔG_0 = 17.5±0.2 pN·nm for poly(A) and 14.0±0.3 pN·nm for poly(C), which now can be directly compared with the free energy change obtained from biochemical ensemble-averaged experiments where only temperature was varied.

5.3.2 Transition kinetics

In addition to the thermodynamic properties, we also investigated the unfolding kinetics of the transition mechanism and obtain the unfolding rate, α_0 at zero force, and the activation barrier width, x_u (Fig. 5.6). We determined the probability, $P(F)$ that the molecule will be unfolded at a given force by averaging series of the fractions

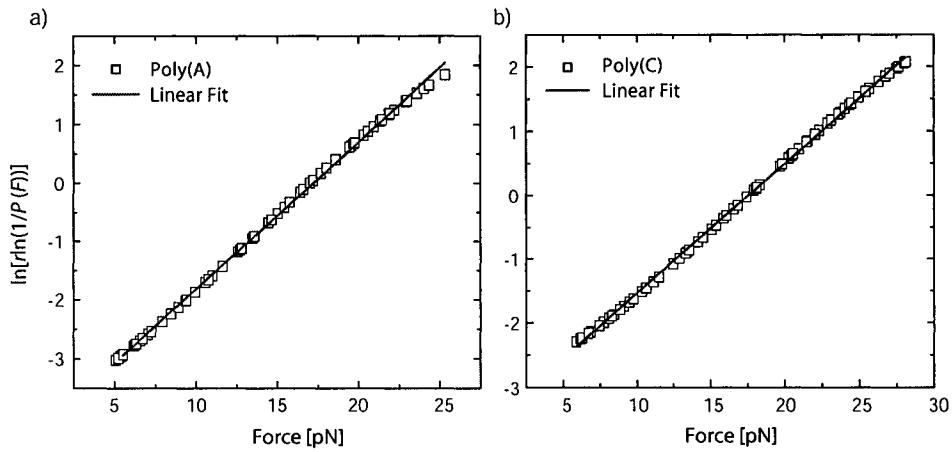

FIGURE 5.6. The unfolding rate calculation by linear fit to $\ln[r\ln(1/P(F))]$ vs force plots. $P(F)$ is obtained by averaging the series of N_1/N vs force curves. a) For poly(A), The loading rate, $r = 5.45$ pN/s. The unfolding rate, α_0 and the activation width for unfolding, x_u are 0.0033/s and 1.02 nm, determined by linear fit. b) For poly(C), $r = 8.17$ pN/s. The obtained α_0 and x_u are 0.0057/s and 0.82 nm respectively.

of the folded domains, N_1/N vs force curves. N_1/N are calculated using Eq. 5.3 and the two-state fitting parameters (Table 5.1). The force-dependent unfolding probability, $P(F)$ was mathematically derived as [33, 79]:

$$P(F) = e^{\frac{\alpha_0 k_B T}{x_u r}(e^{x_u F/k_B T}-1)}. \tag{5.6}$$

It can be approximated in the high force limit($> 3pN$) [33],

$$\ln[r\ln(1/P(F))] = \ln(\alpha_0 k_B T/x_u) + F x_u/k_B T, \tag{5.7}$$

where r indicates the loading rate (pN/s). Using this formula, we fitted to the data and obtained α_0 and x_u. For poly(A), $\alpha_0 = 0.0033$/s and $x_u = 1.02$ nm and for poly(C), $\alpha_0 = 0.0057$/s and $x_u = 0.87$ nm respectively, indicating both helices are quite stable at zero force (at room temperature). If we assume that x_u and x_f remain constant over the change of applied force, x_f can be calculated by subtracting x_u from the contour length changes $(L_2 - L_1)$ which were acquired from the two-state fitting. We find that x_fs for poly(A) and poly(C) are 0.53 nm and 0.52 nm respectively. It

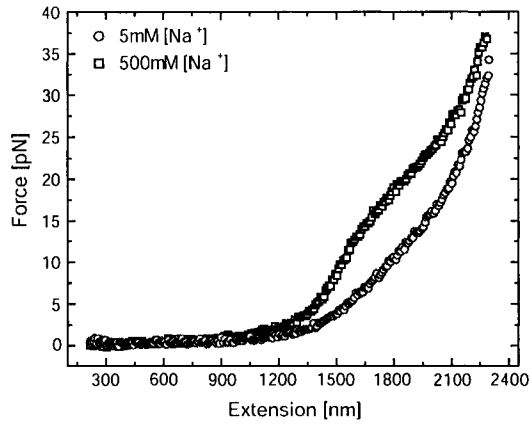

FIGURE 5.7. Force-vs-extension data of poly(C) at 5 mM and 500 mM [Na^+]. The same poly(C) molecule was stretched in two different conditions (5 mM and 500 mM [Na^+]) to investigate the ionic strength effects on the molecular structural conformations. The lack of enough shielding charges results in increasing the persistence length of poly(C) at 5 mM [Na^+] and decreasing the free energy difference between two state. The pronounce kink around 17-20 pN at 500 mM [Na^+] becomes invisible at 5 mM [Na^+].

indicates that the potential for poly(A) is slightly asymmetric than that of poly(C). However, it does not contributes significantly since the relaxation traces of poly(A) are well aligned with its extension traces (data not shown).

5.3.3 Ionic effects

Electrostatic interactions between unshielded negatively charged phosphate groups generally stiffen the molecule causing the persistence length to increase. Especially, the electrostatic interactions becomes important when the Debye screening length λ_D is of the order of or larger than the intrinsic elastic persistence length. Previously, the ionic effects on the elastic properties of poly(U) were studied and found that the elastic properties of the poly(U) cannot be described by models based on the non-self-avoiding chain. We showed that a modified worm like chain model which includes long range interactions of negative charged phosphates have a better agreement with the data acquired at low ionic concentration than a classic WLC [80]. Poly(A) and

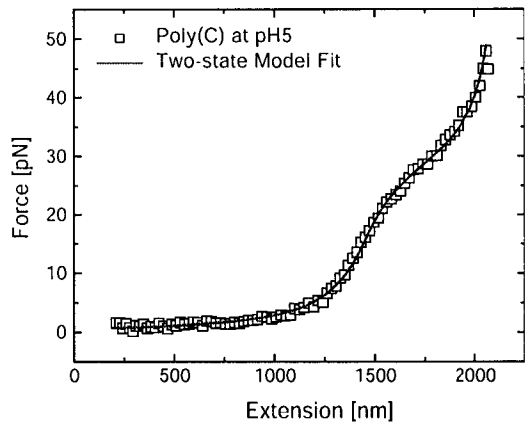

FIGURE 5.8. The force vs extension data of poly(C) at pH 5.0. The data does not show any significance difference compared to those at pH 7.0. Based on the two state-fit, L_1=3.3 nm, L_2=4.6 nm, $L_{p,1}$=1.9 nm, $L_{p,2}$=0.8 nm, ΔG_0 = 21.8 pN·nm, and the total contour length, L = 2396.8 nm. This fitting result does not support the fact that poly(C) forms a double helix at acidic condition.

poly(C) regardless of their states as either helices or random coils are highly affected by the Na^+ concentration. First, the persistence lengths of both polymers increase as we can see in Fig. 5.7: smaller forces are required to stretch to the same amount of extensions with lower Na^+ concentration. Second, the kinks are almost ignorably weak which may be interpreted as recessed transition free energy between two states. It is a reasonable assumption that the electrostatic interactions in the phosphodiester backbone affect base stacking interactions between consecutive bases and subsequently lower the unfolding barrier height. Furthermore a modified WLC model as used in fitting the force-vs-extension data of poly(U) at low salt concentrations does not fit to that of poly(C) (data not shown) indicating under these circumstances poly(C) may still contain considerable amounts of helical domains.

5.3.4 pH effects

We found that the conformations of poly(A) and poly(C) are not affected by pH changes. As shown in Fig. 5.8, force-vs-extension data of poly(A) and poly(C) are

well described by the two-state model, which indicates that the molecules are still in single stranded helical states. Previous studies showed that poly(A) and poly(C) were able to form double helical structures in acidic conditions (less than pH 4.0) [44]. The reason for this discrepancy may lie in the details of sample preparations. First, we used very small concentration of RNA molecules (0.25 to 10 nM) compared to the amounts used (0.1 M) in the previous experiments. Second, we could not lower the pH condition less than 4.5 due to severe aggregations of beads - most likely due to surface-blocking materials (BSA). As a result, RNA molecules might not be able to form double stranded helices.

5.4 Conclusion

Our study showed that poly(A) forms a helical structure with 9 bases as theoretically predicted. For poly(C), the conformation of the molecule is close to a single-stranded helix with 8 bases per turn from NMR experiment rather than 6 bases from X-ray fiber diffraction experiment. The molecules folding and unfolding processes are fully reversible which indicates that stretching did not drive them off from equilibrium. We performed several different methods to calculate rate constants and activation barrier widths. The results are consistent to each other and only slightly differ within error ranges. In general, it is thought that the base-stacking energy is a main source to render a single stranded helix. The base stacking energy for poly(A) is predicted as $\sim$ 0.4 Kcal/mol which corresponds to 25.0 pN·nm for one helical pitch. The base stacking energy for poly(C) is expected to be slightly lower than that of poly(A). Unfortunately, we could not find any references for the base-stacking energy for poly(C). If we assume the base-stacking energy for poly(C) is the same as that of poly(A), the energy corresponding to one pitch is about 22 pN·nm. They are slightly larger than our data (20.2$\pm$0.3 pN·nm and 17.5$\pm$0.8 pN·nm) from the two-state fitting. We calculate the ΔG_0 per base, for poly(A) as 0.34 Kcal/mol

and for poly(C) as 0.32 Kcal/mol, which indicates that the base-stacking energy for poly (C) is not much different from that of poly(A).

Appendix A

PROTOCOLS

A.1 Synthesis of homopolymer

(Caution: RNA is very susceptible to Rnases. Please wear gloves (not necessarily sterilized one) and only use Rnase-free purified water, buffers and items.)

1. **Materials**

   - 2X elongation buffer
     - Tris-HCl (Sigma) 100 mM (pH 9.1 for poly(A), pH 8.2 for poly(C)) and poly(U)
     - DTT (Beringel-Manheim) 2 mM
     - EDTA (Sigma) 2 mM
     - KCl (Sigma) 1.2 M
     - $MgCl_2$ (Sigma) 15 mM
   - RNA oligo (5'-biotinylated 20 mer, Dharmacon) to be elongated
   - Polynucleotide phosphorylase 0.2 unit/μl (Sigma, P2869)
   - ADP, CDP, UDP (Sigma)
   - Eppendorf tubes (1.5 ml nuclease free, Eppendorf), Hot block or Incubator

2. **Elongation step**

   (a) Poly(A)

   1. Add 2.0 mg of ADP into 1.5 ml Rnase-free eppendorf tube
   2. Add 100 μl of 2X elongation buffer and mix well using a vortex
   3. Add 2500 pmol of oligo RNA

4. Add 5 μl of enzyme
5. Add Water up to 200 μl
6. Incubate the tube 55.5 °C for 1 hour (the elongation rate is very fast, the most of oligos are elongated more than 10 kb).

(b) Poly(C)

1. Add 2.5 mg of CDP into 1.5 ml Rnase-free eppendorf tube
2. Add 100 μl of 2X elongation buffer (Use pH 8.2 Tris-HCl buffer) and mix well
3. Add 500 pmol of oligo RNA
4. Add 5 μl of enzyme
5. Add Water up to 200 μl
6. Incubate the tube 39 °C for at least 3 hours to grow to obtain a thick band at 5 kb-7 kb long in the gel

(c) Poly(U)

1. Add 13.0 mg of UDP into 1.5 ml Rnase-free eppendorf tube
2. Add 100 μl of 2X elongation buffer (Use pH 8.2 Tris-HCl buffer) and Mix well
3. Add 500 pmol oligo RNA
4. Add 5 μl of enzyme
5. Add Water up to 200 μl
6. Incubate the tube 39 °C for at least 3 hours to grow to obtain a thick band at 6 kb-8 kb long in the gel

3. **Purification step**

(a) In order to decrease the sample volume, use ethanol precipitation by adding 750 ml of icy cold ethanol (usually keep it in the -20 °C freezer) to the

sample tube and mix by gently flipping the tube upside down several times and put it in the -20 °C freezer for at least 1 hour.

(b) Take the tube out and centrifuge for 5 min at 10 krpm.

(c) Remove supernatant by tilting the tube and carefully pipet out any remained supernatant. At that time try not to touch RNA pellet (if RNA chains are very long, they become very sticky, especially poly(A))

(d) Add 80 μl of Rnase-free water to the tube and gently shake the tube to dissolve the pellet (they should be dissolved very quickly, otherwise, the pellet is not RNA)

(e) In order to get rid of any remaining protein and NDPs, RNA purification kit (Quiagen) or other commercial RNA purification kits should be used.

(f) After purification, quantify the concentration using the spectrometer and run a 1 % RNA gel to estimate the length of RNA

4. **3'-end labeling with Digoxigenin**

- Use the terminal transferase from Invitrogen (Terminal transferase from Roche contains something which degrades RNA, NEB usually makes good enzymes except for terminal transferase - the efficiency is very bad.)
- Follow the protocol and use the buffer which comes with terminal transferase.

A.2 Coating Beads with anti-Digoxygenin

1. **Materials**

- Aldehyde-sulfate beads (0.49 μm, Interfacial Dynamics)
- 1X PBS buffer (pH 7.2) (10X PBS tablet, Calbiochem)

- Acetylated BSA (Sigma)
- Glycine (Sigma)
- two Eppendorf tubes (1.5 ml nuclease free, Eppendorf)
- Rotator

2. **Procedures**

(a) Two 1.5 ml tubes are incubated with 1.2 ml 2 mg/ml BSA in PBS buffer for two hours with constant gentle mixing.

(b) Empty and rinse tubes twice with Rnase-free water and then drain them.

(c) Add 0.6 ml of 4.1 %(w/v) 0.49 μm beads and 0.6 ml PBS buffer to one of the tubes and vortex for 30 sec

(d) Spin down beads for 2 min at 13 krpm.

(e) Discard supernatant and re-suspend beads in 1.2 ml PBS buffer by vortexing.

(f) Repeat 5 twice more and re-suspend beads in 0.935 ml PBS buffer and vortex for 30 sec

(g) Add 600 μl of 1 mg/ml anti-Digoxigenin fragments to the above tube and mix by pipeting the solution up and down.

(h) Add 80 μl of 1 mg/ml acetylated-BSA and mix by vortexing for 30 sec

(i) Stay overnight with constant gentle mixing at room temperature.

(j) Spin down beads for 2 min at 13 krpm.

(k) Discard supernatant and re-suspend in 1.2 ml 1.0 M glycine in PBS buffer.

(l) Incubate it for 40 min at room temperature with constant gentle mixing.

(m) Spin down and re-suspend it in 960 μl PBS and add 40 μl of 80 mg/ml Acetylated BSA and 5 μl of 2 % (w/v) sodium-azide.

(n) Transfer bead suspension to the second BSA treated tube from the first step.

A.3 Preparation for RNA stretching

A.3.1 Preparation of Sample cells

1. Prepare precleaned microslides (VWR), streptaividin coated cover glass (Xenopore), and epoxy (Falcone).
2. Put a microslide on a paper with grid. (This grid helps to attach a cover glass to the center of a microslide.
3. First put two spacer (white, 2 mm X 25 mm X 1/64 in, (width, height, thickness), Grainger) where the edges of a cover glass sit on and apply two thin strips of epoxy just inner sides of spacers.
4. Carefully put a cover glass on the top of spacers and place it in a petri dish with a top.
5. Cover the petri dish with wax paper and put a cover.
6. Store it at 4 °C. Once it is made, it will be okay for a week.

A.3.2 Tethering Anti-digoxigenin beads with RNA

1. Add 4 μl of 0.32 nM anti-digoxigenin beads (12.8 fmole) to a 1.5 ml eppendorf tube containing 50 μl incubation buffer (4 mM Hepes, pH 7.0, 500 mM NaCl)
2. Add 2.5 μl of 20 mg/ml Ac-BSA.
3. Vortex for 15 to 30 s.
4. Add 26 fmole to 128 fmole of differentially labeled RNA.

5. Add water up to 100 μl.

6. Incubate the tube at 4 °C for overnight.

A.3.3 Tethering RNA with beads to a streptavidin coated surface

1. Take out a sample cell stored at 4° C fridge and sit it at the room temperature for 30 min.

2. Flow 100 μl of a desired buffer (however it should contains enough Na^{+} or Mg^{2+}) with 0.5% w/v Ac-BSA containing buffer.

3. Sit it for 1 hour at room temperature.

4. Introduce RNA and bead mixture and sit it for 30 min.

5. Wash any unbound beads by flowing 500 μl of a desired buffer that you wish to work with.

References

[1] F. Crick, Central dogma of molecular biology, Nature, 227 561 (1970)

[2] B. Alberts, A. Johnson, J. Lewis, M. Raff, K. Roberts, P. Walter, Molecular Biology of the Cell. Garland Pub; 4th edition (March 2002)

[3] H. Yin, M.D. Wang, K. Svoboda, R. Landick, S.M. Block, and J. Gelles, Transcription against an applied force, Science, 270 1653 (1995)

[4] N.H. Tompson, B.L. Smith, M. Almqvist, L. Schmitt, M. Kashlev, E.T. Kool and P.K. Hansma, Oriented, active *Escherichia coli* RNA polymerase: an atomic force microscopy study, biophys. J. 76 1024 (1999)

[5] Y. Harada, O. Ohara, A. Takatsuki, H. Itoh, N. Shimamoto, and K. Kinosita Jr, Direct observation of DNA rotation during transcription by *Escherichia coli* RNA polymerase, Nature, 409 113 (2001)

[6] M.D. Wang, M.J.Schnitzer, H. Yin, R. Landick, J. Gelles, and S.M. Block, Force and velocity measured for single molecules of RNA polymerase. Science 282 902907 (1998)

[7] G.J. Wuite, S.B. Smith, M. Young, D. Keller, and C. Bustamante, single molecule studies of the effect of template tension on T7 DNA polymerase activity. Nature 404, 103 (2000)

[8] J.E. Molloy, J.E. Burns, J. Kendrick-Jones, R.T. Tregear, and D.C. White, Movement and force produced by a single myosin head, Nature, 378 209 (1995)

[9] K. Svoboda, and S.M. Block, Force and velocity measured for single kinesin molecules, Cell, 77 773 (1994)

[10] K. Visscher, M.J. Schnitzer, and S.M. Block, Single kinesin molecules studied with a molecular force clamp, Nature 400, 184 (1999)

[11] M.V. Rodnina, H. Stark, A. Savelsbergh, H.-J. Wieden, D. Mohr, N.B. Matassova, F. Peske, T. Daviter, C.O. Gualerzi, and W. Wintermeyer, . GTPase mechanisms and functions of translation factors on the ribosome. Biol. Chem. 381 377 (2000)

[12] J. Czworkowski, and P.B. Moore, The conformational properties of elongation factor G and the mechanism of translocation. Biochemistry 36 10327 (1997)

[13] D. Keller, and C. Bustamante, The mechanochemistry of molecular motors. Biophys. J. 78 541 (2000)

[14] W. Wintermeyer, and M.V. Rodnina, Translational elongation factor G: A GTP-driven motor of the ribosome. Essays Biochem. 35 117 (2000)

[15] K. Kinosita Jr., Real time imaging of rotating molecular machines. FASEB J. 13 S201S208 (1999)

[16] A. Ishijima, and T. Yanagida, Single molecule nanobioscience. Trends Biochem. Sci. 26 438 (2001) molecular motors.

[17] T. Strick, J.-F. Allemand, V. Croquette, and D. Bensimon, Twisting and stretching single DNA molecules. Prog. Biophys. Mol. Biol. 74 115140 (2000)

[18] A. Ashkin, Forces of a single-beam gradient laser trap on a dielectric sphere in the ray optics regime, Biophys. J., 61 569 (1992)

[19] K. Svoboda, and S. Block, Biological applications of optical forces, Annu. Rev. Biomol. Struct. 23 247 (1994)

[20] K. Visscher, S. Gross, and S. Block, Construction of multiple -beam optical traps with nanometer resolution position sensing, IEEE Sel. Topics Quantum. Electron, 2 1066 (1996)

[21] J.M.G Vilar and J.M. Rubi, Noise suppression by noise, Phys. Rev. Lett. 86, 950 (2001)

[22] D.B. Walton and K. Visscher (accepted in PRE)

[23] R. D. Astumian, Thermodynamics and Kinetics of a Brownian Motor, Science, 276, 917 (1997)

[24] Y. Okada, N. Hirokawa, A Processive Single-Headed Motor: Kinesin Superfamily Protein KIF1A, Science 283, 1152 (1999)

[25] D.F. Russell, L.A. Wilkens, F. Moss, Use of behavioural stochastic resonance by paddle fish for feeding, Nature 402, 291 (1999)

[26] R. Benzi, G. Parisi, A. Sutera, and A. Vulpiani, Stochastic resonance in climatic change, SIAM J. Appl. Math. 43, 565 (1983).

[27] P. Hänggi, Chemphyschem, 2002, 285 (2002)

[28] M.B. Priestley, Academic Press, Spectral Analysis and Time Series (1981)

[29] K. Visscher, S.M. Block, Versatile optical traps with feedback control, Meth. Enzymol. 298 460 (1998)

[30] R.M Simmons, J.T. Finer, S. Chu S., J.A Spudich, Quantitative measurements of force and displacement using an optical trap, Biophys J. 70 1813 (1996)

[31] H.A. Kramers, Brownian motion in a field of force and a diffusion model of chemical reactions. Physica 7, 284 (1940)

[32] L. Gammaitoni, P. Hänggi, P. Jung, F. Marchesoni, Stochastic resonance. Rev. Mod. Phys. 70, 223 (1998)

[33] J. Liphardt, B. Onoa, S.B. Smith, I. Tinoco, and C. Bustamante, Reversible unfolding of single RNA molecules by mechanical force. Sciecne 292, 733 (2001)

[34] A. Simon, and A. Libchaber, Escape and synchronization of a Brownian particel. Phys. Rev. Lett. 68, 3375 (1992)

[35] L.I. McCann, M.I. Dykman, and B. Golding, Thermally activated transitions in a bistable three-dimensional optical trap. Nature(London) 402, 785 (1999)

[36] R.S. Maier and D.L. Stein, Noise-Activated Escape from a Sloshing Potential Well. Phys. Rev. Lett.86, 3942 (2001)

[37] M.H. Choi, R.F. Fox, and P. Jung, Quantifying stochastic resonance in bistable systems: Response vs residence-time distribution functions. PRE 57, 57 (1998)

[38] V.N. Smelyanskiy, M.I. Dykman, and B.Golding, Time oscillations of escape rates in periodically driven systems. Phys.Rev.Lett. 82, 3193 (1999)

[39] J. Lehmann, P. Reimann, and P. Hänggi, Surmounting Oscillating Barriers. Phys. Rev. Lett. 84, 1639 (2000)

[40] M.I. Dykman, D.G.Luchinsky, R. Mannella, P.V.E. McClintock, N.D. Stein, and N.G. Stocks, Nuovo Cimento D 17, 661 (1995)

[41] J.F. Marko, E.D. Siggia, Stretching DNA. Macromolecules 28, 8759 (1995)

[42] S. Cocco, R. Monasson, J. Yan, A. Sarkar, and J.F. Marko, Force-extension behavior of folding polymers. Euro. Phys. J. 10, 249 (2003)

[43] M. Grunberg-Manago, P.J. Ortiz, S. Ochoa, Enzymic synthesis of polynucleotides. I. Polynucleotide phosphorylase of azotobacter vinelandii. Biochim Biophys Acta. 1, 269 (1956)

[44] W. Scovell, Structural and conformational studies of polyriboadenylic acid in neutral and acid solution. Biopolymers 17 969 (1978)

[45] E.O. Akinrimisi, C. Sander, and P.O.P Ts'o, Properties of helical polycytidylic acid. Biochemistry 2 340 (1963)

[46] G.D. Fasman, C. Lindblow, and L. Grossman, The helical conformations of polycytidylic acid: studies on the forces involved. Biochemistry 3 1015 (1964)

[47] J.C Thrierr, M. Dourlent, and M. Leng, A study of polyuridylic acid. J. Mol. Biol. 58, 815 (1971)

[48] E.G. Richards, C.P. Flessel and J.R. Fresco, Biopolymers 1, 431 (1963)

[49] H. Simpkins and E.G. Richards, Biopolymers 5 551 (1967)

[50] M. Leng, and G. Felsenfeld, A study of polyadenylic acid at neutral pH. J. Mol. Biol. 15, 455-466 (1966)

[51] J. Brahms, A.M. Michelson, and K.E.Van Holde, Adenylate oligomers in single- and double-strand conformation. J. Mol. Biol. 15, 467-488 (1966)

[52] C. Haasnoot, and C. Altona, A conformational study of nucleic acid phosphate ester bonds using phosphorus-31 nuclear magnetic resonance. Nucleic. Acid. Res. 6, 1135 (1979)

[53] B. Maier, D. Bensimon, and V. Croquette, Replication by a single DNA polymerase of a stretched single-stranded DNA. Proc. Natl. Acad. Sci. U.S.A. 97, 12002 (2000)

[54] T.R. Strick, J.F. Allemand, D. Bensimon, A. Bensimon, V. Croquette, Single molecule analysis of DNA uncoiling by a type II topoisomerase. Nature 404, 901 (2000)

[55] S.B. Smith, Y. Cui, C. Bustamante, Overstetching B-DNA the elastic response of dsDNA and ssDNA molecule. Science 271, 795 (1996)

[56] M.D. Wang, H. Yin, R. Landick, J. Gelles, and S.M. Block, Stretching DNA with optical tweezers. Biophys. J. 72, 1335 (1997)

[57] C. Bouchiat, M.D. Wang, J. Allemand, T. Strick, S.M. Block, and V. Croquette, Estimating the persistence length of a worm-like chain molecule from force-extension measurements. Biophys. J. 76, 409 (1999)

[58] W. Saenger, J. Riecke, and D. Suck, A structural model for the polyadenylic acid single helix. J. Mol. Biol. 93 529 (1975)

[59] C. Bauman, S. Smith, V. Bloomfield, and C. Bustamante, Ionic effects on the elasticity of single DNA moleculeProc. Natl. Acad. Sci. USA 94, 6185 (1997)

[60] J. Wenner, M. Williams, L. Rouzina, and V. Bloomfield, Salt dependencecof the elasticity and overstretching transition of single DNA molecule. Biophys. J. 82, 3160 (2002)

[61] T. Odijk, J. Polym. Sci. 15 944 (1977)

[62] J. Skolnick and M. Fixman, Macromolecules 10 944 (1977)

[63] J. Barrat and J. Joanny, persistence length of polyelectrolyte chains. Europhys. Lett. 24, 333 (1993)

[64] C.R. Cantor, and P.R. Schimmel, Biophysical Chemistry, PartIII: The behavior of biological macromolecues. W.H. Freemann, San Francisco (1980)

[65] M.E. Fisher, Magnetism in one-dimensional systems - Heigenberg model for infinit spin. Am. J. Phys., 32 343 (1964)

[66] M.-N. Dessinges, B. Maier, Y. Zhang, M. Peliti, D. Bensimon, and V. Croquette, Stretching ssDNA, a model polyelectrolyte. Phys. Rev. Lett. 89, 248102-1 (2002)

[67] Y. Zhang, H. Zhou, and Z.-C. Ou-Yang, Stretching single-stranded DNA: Interplay of electrostatic, base-pairing, and base-stacking interactions, Biophys. J. 81, 1133 (2001)

[68] A.Y. Grosberg, T.T. Nguyen, and B.I. Shklovskii, Rev. Mod. Phys. 74, 329 (2002)

[69] S.B. Zimmerman, J. Mol. Biol. 101, 563 (1976)

[70] J.R. Fresco, Polynucleotides. II. The X-ray diffraction patterns of solutions of he randomly coiled and helical forms of polyadenylic acid. J. Mol. Biol. 1, 106 (1959)

[71] M.S. Broido and D.R. Kearns, ^{1}H NMR evidence for a left-handed helical structure of poly(ribocytidylic acid) in neutral solution. J. Amer. Chem. Soc. 104, 5207 (1982)

[72] B. Zmudzka, C. Janion, and D. Shugar, Poly 2'-O-methylcytidylic acid and the role of the 2'-hydroxyl in polynucleotide structure. Biochem. Biophys. Res. Commun. 37, 895 (1969)

[73] J. Alderfer, I. Tazawa, S. Tazawa, and P.O.P. Ts'o, Comparative studies on polydeoxyribocytidylate (dC), polycytidylate (rC) and poly-2'-O-methylcytidylate (mC) and polydeoxyriboinosinate (dI), polyiboinosinate (rI) and poly-2'-O-methylriboinosinate (mI). Biophys. J. 15, 29a (1975)

[74] A.G. Leslie, and S. Arnott, Structure of single-stranded polyribonucleotide poly(2'-O-methylcytidylic acid). J. Mol. Biol. 119, 399 (1978)

[75] K.C. Neuman, E. Abbondanzieri, T.T. Perkins, and S.M. Block, Determining relative and axial displacement in optical traps Biophys. J. 80 163A. (2001)

[76] M. Rief, J. Fernandez, and H. Gaub, Elastically coupled two-level systems as a model for biopolymer extensisbility. Phys. Rev. Lett. 81, 4764-4767 (1998)

[77] I. Schwaiger, C. Sattler, D.R. Hostetter,and M. Rief, The myosin coiled-coil is truly elastic protein structure, Nature Materials 1, 232-235 (2002)

[78] S. Cocco, J.F. Marko, and R. Monasson, Theoretical models for single molecule DNA and RNA experiments : from elasticity to unzipping, C.R. Physique 3 569 (2002)

[79] E. Evans, and K. Ritchie, Strength of a weak bond connecting flexible polymer chains. Biophy. J. 72, 1541 (1997)

[80] Y. Seol, G.M. Skinner, and K. Visscher, Elastic properties of a single-stranded charged homopolymeric ribonucleotide. (to be published)